REPORT DOCUMENTATION PAGE

PLEASE DO NOT RETURN YOUR FORM TO THE ABOVE ORGANIZATION.

1. REPORT DATE	2. REPORT TYPE	3. DATES COVERED	
20221130	Conference Paper	START DATE 20221017	END DATE 20221130

4. TITLE AND SUBTITLE

Applying Deep Eutectic Solvent and Solvated Ionic Liquid Concepts to Energetics

5a. CONTRACT NUMBER	5b. GRANT NUMBER	5c. PROGRAM ELEMENT NUMBER
5d. PROJECT NUMBER	5e. TASK NUMBER	5f. WORK UNIT NUMBER Q27T

6. AUTHOR(S)

Stefan Schneider

7. PERFORMING ORGANIZATION NAME(S) AND ADDRESS(ES) Air Force Research Laboratory (AFMC) AFRL/RQRP 10 E. Saturn Blvd Edwards AFB, CA 93524-7680	8. PERFORMING ORGANIZATION REPORT NUMBER

9. SPONSORING/MONITORING AGENCY NAME(S) AND ADDRESS(ES) AFRL/RQR 5 Pollux Drive Edwards AFB, CA 93524-7048	10. SPONSOR/MONITOR'S ACRONYM(S) AFRL/RQR	11. SPONSOR/MONITOR'S REPORT NUMBER(S) AFRL-RQ-ED-TR-2022-287

12. DISTRIBUTION/AVAILABILITY STATEMENT

Distribution Statement A: Approved for Public Release; Distribution Unlimited. PA Clearance Number: AFRL-2022-5646
Clearance Date: 21 Nov 2022

13. SUPPLEMENTARY NOTES

For presentation at AFOSR final FT 19-22. The U.S. Government is joint author of the work and has the right to use, modify, reproduce, release, perform, display, or disclose the work.

14. ABSTRACT

15. SUBJECT TERMS

N/A

16. SECURITY CLASSIFICATION OF:			17. LIMITATION OF ABSTRACT	18. NUMBER OF PAGES
a. REPORT Unclassified	b. ABSTRACT Unclassified	C. THIS PAGE Unclassified	SAR	53

19a. NAME OF RESPONSIBLE PERSON	19b. PHONE NUMBER (Include area code)
Stefan Schneider	N/A

PREVIOUS EDITION IS OBSOLETE.

STANDARD FORM 298 (REV. 5/2020)
Prescribed by ANSI Std. Z39.18

LRIR #: 20RQCOR034

Title: **Applying Deep Eutectic Solvent and Solvated Ionic Liquid Concepts to Energetics**

Reporting Period: 01 October 2019 – 30 September 2022

Laboratory Program Manager and
Laboratory Principal Investigator: Dr. Stefan Schneider

Commercial Phone: (661) 275 5759, DSN: 525 5759

FAX: (661) 275 5471

Mailing Address: 10 E. Saturn Blvd, Bldg 8451
Edwards AFB, CA 93524-7680

E-Mail Address: stefan.schneider@spaceforce.mil

AFOSR Program Manager: Dr. Michael R. Berman

TABLE OF CONTENTS

1.0 TASK I: Applying Deep Eutectic Solvent and Solvated Ionic Liquid Concepts to EnergeticsTechnical Objective Task I: Deep Eutectic Solvents

Although the DES concept was originally employed to provide an understanding of the unique properties of unusual salt/solvent mixtures, it appears to have special relevance to the production of new energetic materials. Solids with extremely high melt points can be combined with neutral materials with moderately high melt points to produce free-flowing liquids with melt points low enough to meet operability requirements for liquid fuels. The weakening, breaking, and rearrangement of intermolecular hydrogen bonds between the constituents and even the possibility of new proton-exchanged species seems especially rich, and it is not yet understood what the impacts are for the resulting liquid.

- The same hydrogen-bond changes which promote the formation of a DES seem to be associated with an increase in overall sensitivity in many systems. We will investigate the effect of neutral-to-salt ratios upon the phase diagram of these mixtures and the relative contribution of the hydrogen-bond donor (HBD) and hydrogen-bond acceptor (HBA) towards sensitivity.
- Our preliminary results caution against premature assessment of the long-term thermal stability of a DES from initial DSC and TGA experiments, a fact already discovered in some choline chloride systems, but this phenomenon has not been sufficiently explained. We will analyze thermal stabilities in detail, distinguishing between evaporative and decomposition instabilities as a function of neutral-to-salt ratios.
- Collaborations with theoretical groups are anticipated that will eventually lead toward synthesis being guided by theory, in preference to an isolated classical, empirical approach. Simulations rely on experimental data for validation and tuning of the theoretical models and we will provide central data by investigating single crystal X-ray structures of these highly complex systems whenever possible.
- Besides our own preliminary work, the data available in the context of energetic materials are scarce at best and barely scratch the surface of the potential of this area and more data are needed to explore the accessible chemical terrain. Our experimental strategies are driven to provide a broader database essential to answer key scientific questions.

With more extensive understanding the DES concept could serve as a valuable tool in effectively designed energetics with tailored properties for real world applications.

Characterization of materials includes spectroscopic identification, physical property assessment (such as melting point, boiling point, heat of combustion, density and vapor pressure) and hazard properties (such as impact, friction, and ESD sensitivity; thermal stability; NOL card gap detonability; and material compatibility). Establishing detailed phase diagrams either experimentally and/or theoretically is an important objective of the proposed work.

Furthermore, we will also provide sufficient quantities for collaborative combustion studies with the goal to confirm the theoretical performance potential of the new liquids.

1.2. Technical Objective Task I: Solvated Ionic Liquids (SIL)

Classical examples of SIL are lithium salts dissolved in glymes. They are a much less broadly investigated concept than DES. Applied to propellants, SIL with their unique solvation structure surrounding the cation offer a completely different avenue into new, unconventional energetic liquids. We have been successful obtaining SIL from $LiBH_4$ and simple amines but failed using the more energetically favorable LiB_3H_8 salt.

- Leveraging our extensive experience with "classical" ionic liquids (IL) we will focus on lithium cyano-substituted borohydrides. IL with these type of anions have shown low viscosities together with long liquid range and superior hydrolytic stability, properties we hope to retain in the proposed SIL.
- To sustain a high energy content we will utilize high-energy, nitrogen-containing ligands. We will accomplish a comparative study of the effects of energetic nitrogen ligands on SIL formation with a variety of lithium cyano-substituted borohydride salts.

The initial anions are selected on the basis of literature precedence. Very limited data on corresponding lithium salts are available. Examples of our initial target molecules are shown below.

Solvating Ligands   Lithium Salts
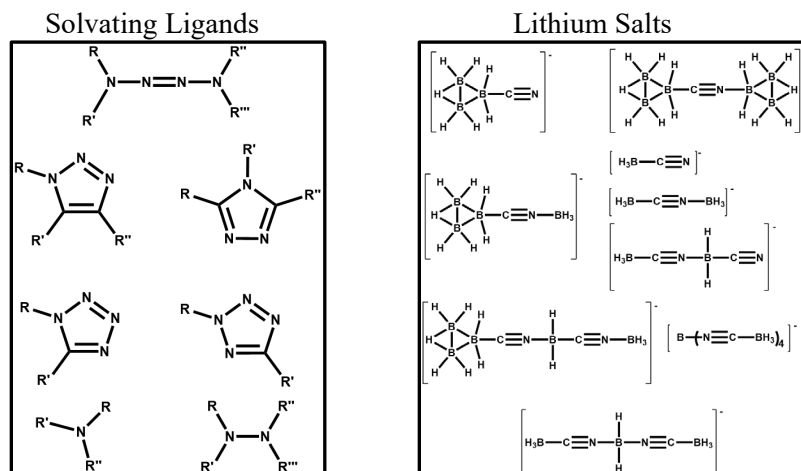
As in case of DES, collaborations with theoretical groups are anticipated eventually guiding the synthesis and the same experimental characterization methods will be employed. This work will not only advance the knowledge of the general coordination chemistry of selected lithium salts but also provide an understanding of the changes in the electronic distribution within the solvated lithium cation which is ultimately responsible for the formation of a liquid SIL.

1.3. Introduction Task I: Deep Eutectic Solvents & Solvated Ionic Liquids

Eutectics have long played a role in propellants and explosives. One of the initiating discoveries (in 1873) was the dissolution of ammonium nitrate in ammonia, later known as Divers solution. Most notable was the observation that the vapor pressure of the ammonia was so reduced that the solution could be handled at room temperature. This work was influential in the search for a suitable melting point depressant for hydrazine. Of special interest was hydrazine nitrate which led to the development of many hydrazine-type fuel blends for bipropellant and monopropellant applications.

During this search the freezing point depression curves for hydrazine were estimated (Figure 1). These curves indicated that the solvation of one or two molecules of hydrazine with one molecule of the additive produced the largest freezing point depression. Thus, to achieve maximum depression the additive should be of such nature that it can form a compound with hydrazine. These compounds might be simple hydrogen-bonded adducts, new salts, or any equilibrium mixture in between. These interactions can be so specific that stoichiometric mole ratios are observed in some mixtures.
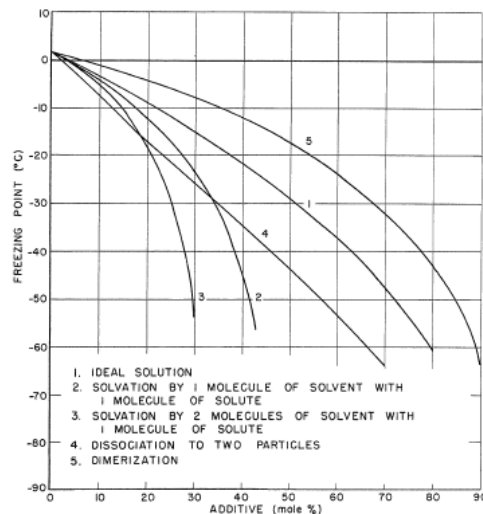
Figure 1. Theoretical freezing point depression of hydrazine with generic solute.

Divers noted that at certain temperatures and pressures ammonium nitrate combined with ammonia at particular stoichiometries but saw no evidence for a new molecular species being formed. Although the hydrogen-bond interactions formed were strong enough to dramatically lower the vapor pressure of the resulting solution, they were insufficient to prevent the neutral base (or solvent) from being easily evaporated leaving behind the uncoordinated salt. While this is not surprising for a solvent with such a low boiling point (-33°C), this effect still posed an operability obstacle for hydrazine blends incorporating hydrazine nitrate. With saturated solutions some hydrazine would be lost during storage or a temperature change could cause the nitrate to precipitate. Furthermore, during combustion experiments it was noted that the more volatile fuel would burn first leaving behind the unsolvated nitrate which could then detonate. To keep the nitrate salts in solution and make them safe to handle many explosive formulations utilized water as an additive. While these solutions became safe to handle, the water content naturally led to degraded performance.

Energetic ILs have been seen as the solution to some of the handling difficulties of the hydrazines, which have a toxicity closely related to their volatility. However, many energetic ILs of interest are considerably more expensive to make and quite difficult to purify. Residual solvent, metal contaminants from metatheses, or unreacted amine serve in a coordinating role, severely depressing the true melting point (mp) of the pure IL.

The DES concept offers opportunities to circumvent problems inherent to ILs by taking advantages of their tendency to strongly associate with neutral molecules. The accepted justification for the eutectic effects is that the complexing agent, typically a protic HBD, interacts with the anion, a HBA. The HBD increases the effective size of the anion, diluting its Coulomb interaction with the cation, and therefore causing a mp depression.

SIL provide a different conceptual avenue into new, unconventional energetic liquids. As our stated threshold for any new liquid propellant is the performance of the hydrazines, many chemically interesting ideas prove inadequate. To validate an ideal specific impulse (Isp), a typical figure of merit for propellants, was calculated. Figure 2 shows the sea level (SL) Isp of selected lithium metal hydride salts, some of which have been used in the past as melt-point depressants for hydrazine. Their performance is optimized with nitrogen tetroxide (NTO) as the oxidizer and plotted as a function of the mass fraction of lithium salt dissolved in hydrazine.
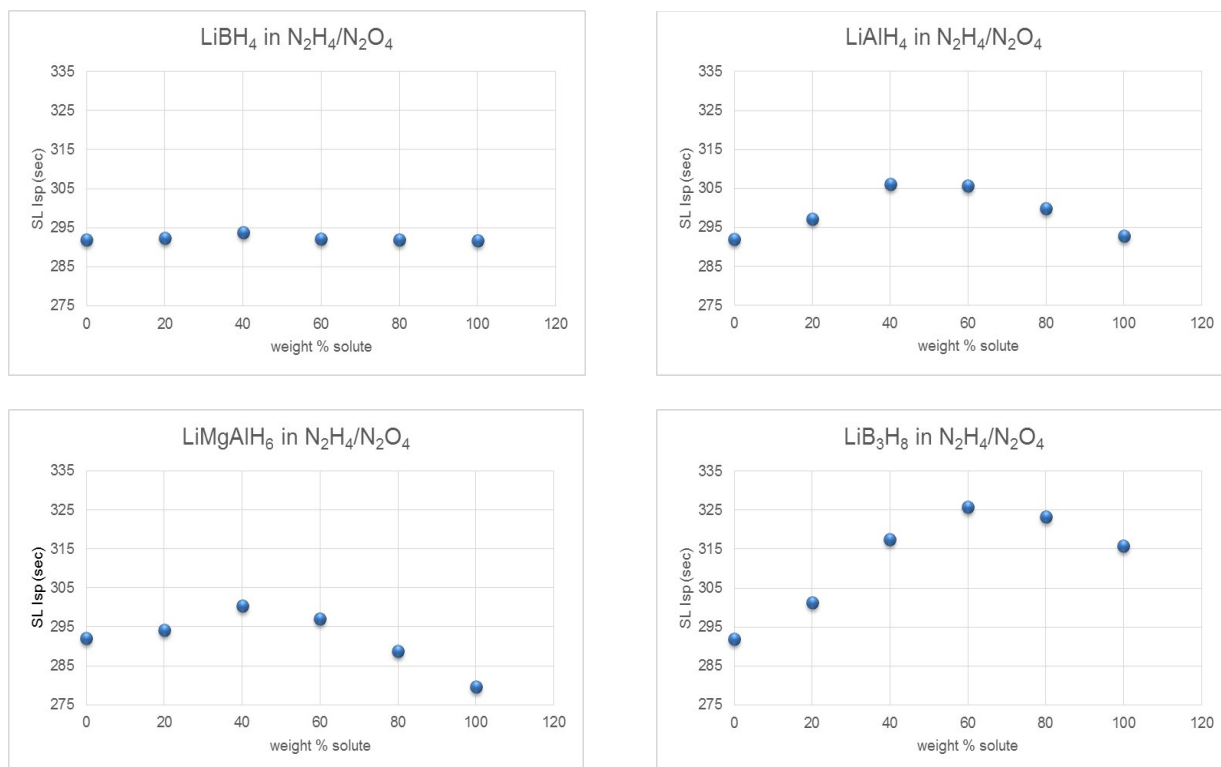
Figure 2. Sea level performance of different lithium metal hydrides in hydrazine optimized with N_2O_4 oxidizer (Pc=1000psi expanded to 14.7 psi)

   Hydrazine/NTO was selected as the representative state-of-the-art propellant since it is almost exclusively employed in our satellite systems today. Furthermore, in the chemical context of our work, hydrazine can be one possible coordinating ligand for the selected lithium metal hydride salts. On the x-axis, 0 weight percent solute represents neat hydrazine and its performance is depicted on the y-axis (Figure 3). At 100% the graphs show the hypothetical performance of the neat lithium metal hydrides. $LiBH_4$ shows almost no improvement over hydrazine at any concentration.
   Previously we obtained the first liquid lithium borohydride SIL with a 2:3 lithium to amine ratio (as determined by ^1H NMR, Figure 3).
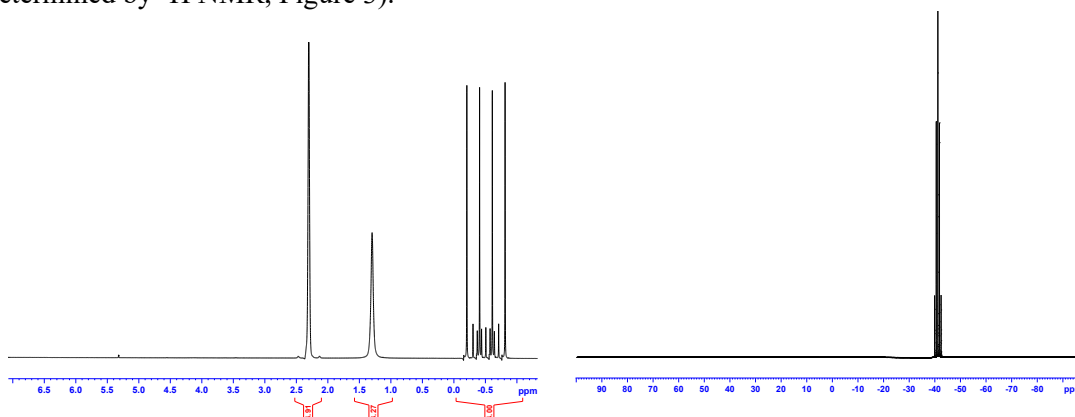
Figure 3. ^1H (left) and ^{11}B (right) NMR of $Li_2(H_2NCH_3)_3(BH_4)_2$.

   This complex showed a melting point of only 4°C and appeared to be thermally stable with no decomposition visible until ~180°C according to DSC data. Upon further analysis by TGA-MS, it was

6

seen that the coordination of the amine was not as strong as initially supposed. The methylamine ligand (mass 31) is almost immediately lost upon heating (Figure 4).
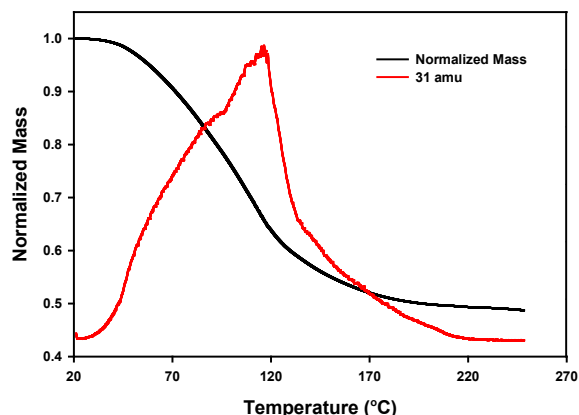
Figure 4. TGA-MS of $Li_2(H_2NCH_3)_3(BH_4)_2$.

The next hydride selected, $LiAlH_4$ (Figure 2), manifests, depending on the complex formed, a slight improvement over hydrazine. The same is true for the more exotic $LiMgAlH_6$ but it in turn shows no improvement over the commercially available $LiAlH_4$. Of all previously considered lithium salts LiB_3H_8 seemed to be the most advantageous. However, we could not obtain any liquid SIL like in the case of $LiBH_4$ and even solid materials prepared lacked the physical properties necessary to be used as propellants.

The electron-withdrawing nature of the cyano moiety reduces the hydridic character of hydrogen bound to boron rendering the anions much more hydrolytically stable than their unsubstituted borohydride parent. Furthermore, ILs with these anions have shown low viscosities together with long liquid ranges and superior hydrolytic stability. Interestingly, the chemistry of lithium salts containing different cyanoborohydride anions have hardly been researched. Even for the simplest lithium salt in this family, $LiBH_3CN$ (synthesized over 65 years ago), there is no detailed structural information available.

1.4 Task I Results: Deep Eutectic Solvents

1.4.1 High nitrogen heterocycles

One of our focal points is to provide high nitrogen heterocyclic compounds and salts with H-bond donor (HBD) and/or acceptor (HBA) capabilities for the preparation of new energetic DES or _Deep Eutectic Propellant_ (DeEP) materials. Initially, specific efforts were focused on tetrazoles with different hydrazine type tethers (Scheme 2). Tetrazoles **3**, **5** and **6** (Scheme 1 and 2) have been previously mentioned, without providing any details regarding their synthesis, characterization and physical properties.

Considering the potential of these nitrogen rich compounds towards energetic DES/DeEP, their synthesis and physical properties were evaluated. A detailed synthesis and characterization of 1-methyl-5-(methyl-hydrazino)-tetrazole **5**, 2-methyl-5-(methylhydrazino) tetrazole **6**, 1-methyl-5-[(1-methylhydrazinyl) methyl] tetrazole **7**, and 2-methyl-5[(1-methylhydrazinyl) methyl] tetrazole **8** was accomplished. Additionally, these tetrazoles were converted to their corresponding nitrate salts **9 -12** by means of Bronsted acid-base reaction with nitric acid and characterized by ^{1}H and ^{13}C NMR spectroscopy and X-ray crystallography. Salts **9** and **12** are viscous liquids, salts **10** and **11** are solids at ambient temperature. The thermal stabilities of all the compounds were evaluated using Differential Scanning Calorimetry (DSC) and Thermogravimetric analysis (TGA). For an initial safety evaluation, the impact sensitivity of **6** and nitrate salt **10** were established.

7

Synthesis details

Replacement of bromine or chlorine atom with hydrazine is an established method and appeared to be a viable approach towards preparation of tetrazoles **5-8**.

In a typical experiment, a mixture of $AlCl_3$ and NaN_3 (1:3 molar ratio) was heated in THF at 60 - 65 °C for 1 - 2 hours. To this warm solution, chloroacetonitrile was added and heating continued for 16 hours. Recrystallization of the crude product from chloroform afforded 5-(chloromethyl)-tetrazoles **1** as a colorless solid (Scheme 1). Refluxing a solution of sodium hydroxide, dimethyl sulfate and **1** overnight resulted in a mixture of 1-methyl-5-(chloromethyl)- tetrazole (**2**) and 2-methyl-5-(chloromethyl)-tetrazole (**3**) in an equal molar ratio. The tetrazole isomers **2** (1,5 isomer) and **3** (2,5 isomer) have different physical properties which allowed for an easy separation by distillation. **3** is a liquid and was distilled off leaving behind isomer **2** as a white solid. The compounds were characterized by NMR spectroscopy and our data agreed with those reported in the literature. It was anticipated that a simple nucleophilic substitution of the chlorine atom of **2** with hydrazine would be a straightforward process to provide 1-methyl-5-(hydrazinomethyl)-tetrazole **5**. However, treating **2** with an equivalent amount of hydrazine gave exclusively the di-alkylated species **4** (Figure 5). A similar dialkylation reaction was also observed during the reaction of **1** with hydrazine. An initial ^{1}H and ^{13}C NMR investigation was not conclusive but indicated that another product than the desired **5** was formed. **4** was unequivocally confirmed by a single crystal X-ray structure determination. To prepare pure tetrazole **5** an excess hydrazine was required (Scheme 2). The compound was characterized by ^{1}H and ^{13}C NMR spectroscopy. The ^{1}H NMR spectrum of **5** in DMSO-d_6 showed a broad peak at δ = 3.80 ppm for the hydrazine protons and single peak for both the methyl and methylene protons at δ = 4.08 ppm. In CD_3CN, the methylene and methyl protons of **5** are resolved as singlets at δ = 4.11 ppm($-CH_2-$) and δ = 4.05 ppm (NCH_3) respectively. The ^{13}C NMR of **5** showed N-CH_3 signal δ = 34.80 ppm and a signal at δ = 46.80 ppm which can be assigned to the methylene carbon ($-CH_2N_2H_3$) neighbouring the hydrazine moiety. Using a similar procedure, the isomers **2** and **3** were either treated with excess hydrazine or monomethyl hydrazine affording tetrazoles **6-8** (Scheme 2). The compounds were characterized by ^{1}H and ^{13}C NMR spectroscopy. The ^{1}H and ^{13}C NMR spectra of tetrazoles **6** is very similar to **5** except that the N-CH_3 signal shifted downfield (^{1}H, δ = 4.30 ppm, ^{13}C, δ = 39.80 ppm). The tetrazoles derived from **3**, regardless of side chain substituents, exhibit a ^{13}C signal for N-CH_3 at δ = 39.4 ppm in DMSO-d_6 and CD_3CN NMR.

Tetrazoles **5-8** with hydrazine and MMH side chains were converted to the corresponding nitrate salts, **9-12**, by means of Bronsted acid base reaction with nitric acid in methanol (Scheme 2). **9-12** were characterized by ^{1}H and ^{13}C NMR spectroscopy.

Scheme 1. Synthesis of 1-methyl and 2-methyl-5-(chloromethyl)-tetrazoles **2** and **3**.
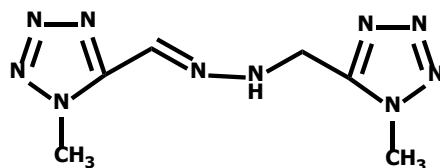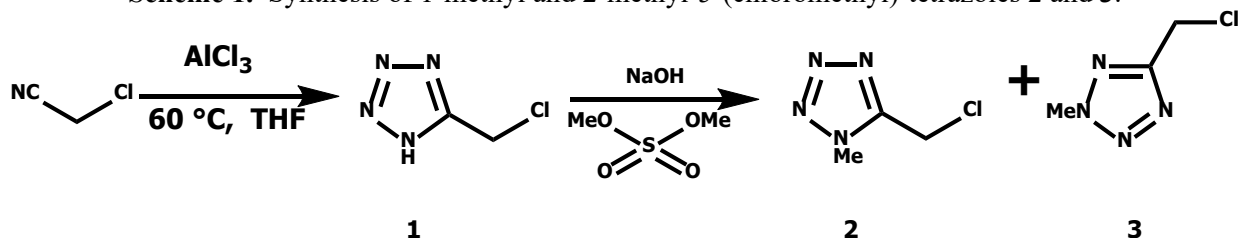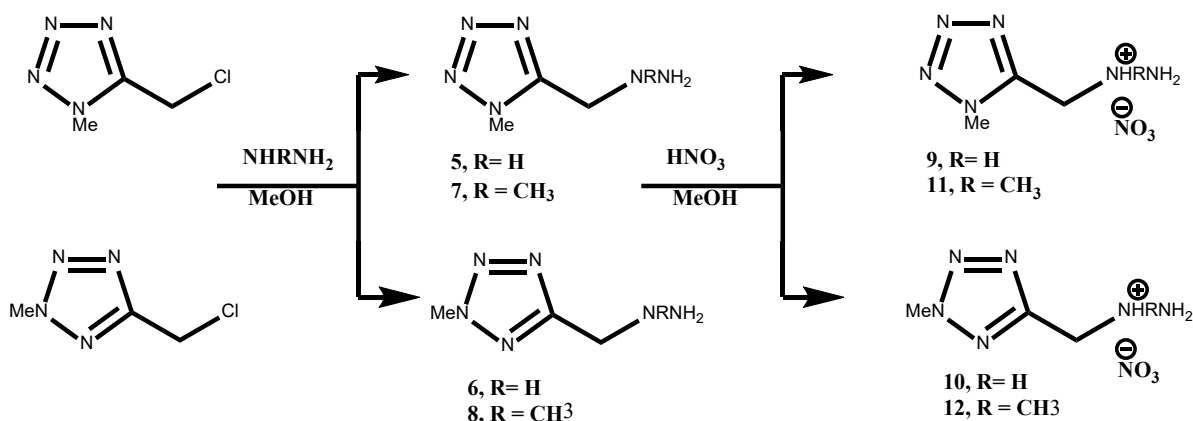

Figure 5. Structure of dialkylation product **4**

**Scheme 2.** Synthesis of tetrazoles **5-8** and their corresponding nitrate salts **9-12**

Physiochemical properties

Melting points, decomposition temperature, viscosities and sensitivity to impact (**6** and **10**) for tetrazoles **5-12** are listed in table 1.

Table 1. Physical and hazard properties of tetrazoles **5-12**.

Compound	Physical State	Viscosity (cP)	T_m (°C)	T_d (°C)	Impact (Kg-cm)
5	Solid	_	37	> 175	
6	Liquid	75 cP	_	>175	> 170
7	Liquid	400 cP	_	> 170	
8	Liquid	105 cP	_	> 150	
9	Viscous liquid	-	-	> 100	
10	solid	_	103	> 200	> 200
11	solid	_	153	> 160	
12	Viscous liquid	-	-	> 100	

The thermal properties of isomeric tetrazoles **5-12** were investigated by DSC (Figure 6) and TGA (Table 1). Tetrazole **5** has a melting temperature of 37 °C with a decomposition onset greater than 170°C, while the tetrazole isomer **6** which is a liquid at room temperature, exhibited no melting point, and a decomposition onset temperature greater than 180°C (Figure 6). Tetrazole isomers **7** and **8** with MMH side chains are both viscous liquids with no detectable melting point and a decomposition onset greater than 170°C.

9
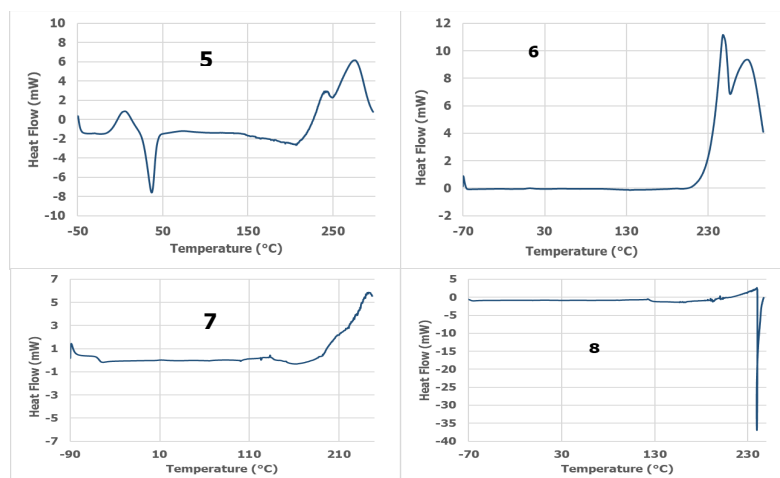
Figure 6. DSC curves of **5-8**

Since all decomposition onsets according to DSC were above 100°C, an isothermal TGA at 75°C for 48h was recorded to get a feel for the different volatilities of the materials (Figure 7). For solid tetrazole **5** a mass loss of less than 4% was noted, while **6** showed a mass loss of greater than 15%. The same trend was observed for the liquid MMH based tetrazoles **7** and **8**. Tetrazole **7** lost about 7% mass while **8** showed a mass loss of more than 50%. After the two-day period the residues left behind from tetrazoles **5-8** were analyzed by ^{1}H NMR spectroscopy and they were identical to the starting materials with no indication of any decomposition. Obviously, the different isomers have quite different volatilities and it should be possible to distill some of these materials at elevated temperatures of at least 75°C under reduced pressure without decomposition. These preliminary TGA indicate that tetrazole **8** is the most volatile.

The nitrate salts **9** and **12** are viscous liquids with no detectable melting point but relatively low decomposition onsets (just >100°C), while **10** and **11** are solids with melting points of 103.0 °C and 153.0 °C respectively. As expected from the DSC measurements, an isothermal TGA of salts **9** and **12** at 75°C for 48h show a mass loss of roughly 9% in both cases, confirming their relatively low thermal stability. Additionally, for an initial safety evaluation, tetrazole **6** and the corresponding nitrate salt **10** were selected for impact sensitivity tests. Both compounds **6** and **10** can be rendered insensitive to impact.
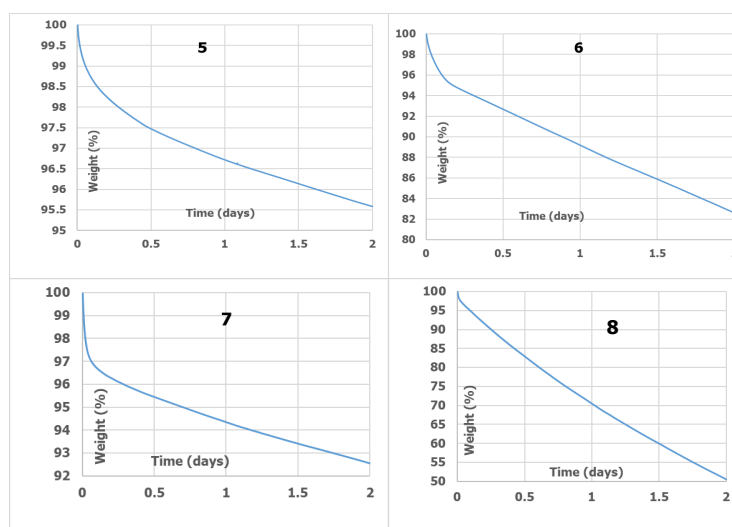
Figure 7. TGA at 75 °C for tetrazole **5 - 8**

10

Based on physical properties, neutral tetrazoles **5** and **6** and nitrate salts **9** and **10** were down-selected for detailed DeEP investigations in combination with neutral hydrazine and the salt 4-amino-1,2,4-triazolium nitrate (4ATNO₃). The initial selection of hydrazine and 4ATNO₃ as DeEP partners was based on our previous experience with these two materials and the successful preparation of numerous DES/DeEP. Schemes 3 and 4 show the general synthesis of DeEPs **1- 4**. We anticipated that in both DeEP **1** and **2**, the salts **9** and **10** function as HBD and hydrazine as HBA. In case of DeEP **3** and **4**, 4ATNO₃ should serve as HBD, while **5** and **6** are HBAs.

DeEP **1-4** were prepared by mixing equimolar ratios of the prospective HBA and HBD inside a glove box (nitrogen atmosphere) in a glass vessel. The glass vessels were sealed with a septum after mixing was done and before they were handled outside the box. The mixtures were heated at 65-80°C for 2 - 6 hours with stirring and the resulting liquids were allowed to cool to room temperature. DeEP **1** produced a glass like material with no visible flow characteristics, DeEP **2** and **4** are both liquids at room temperature, and DeEP **3** is a highly viscous liquid (Figure 8).
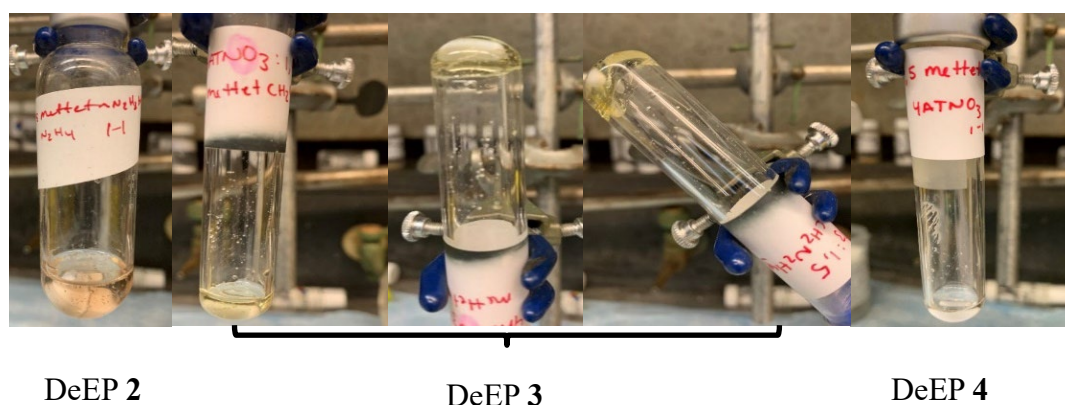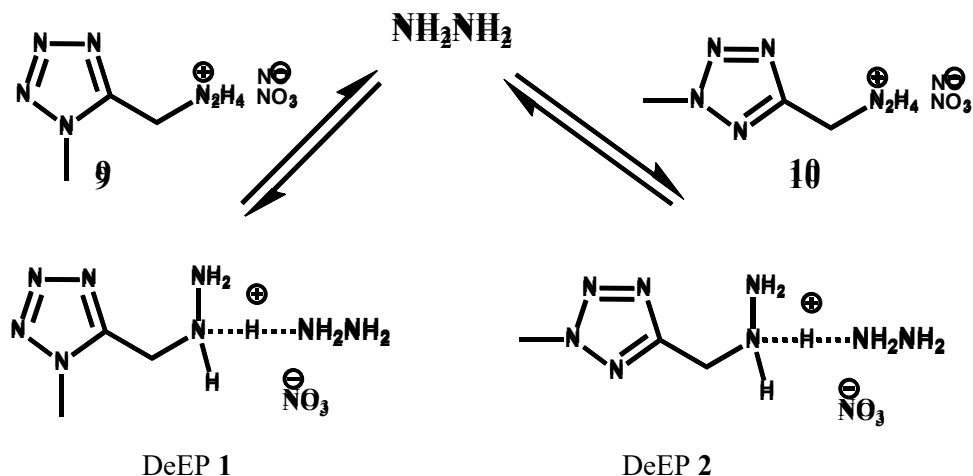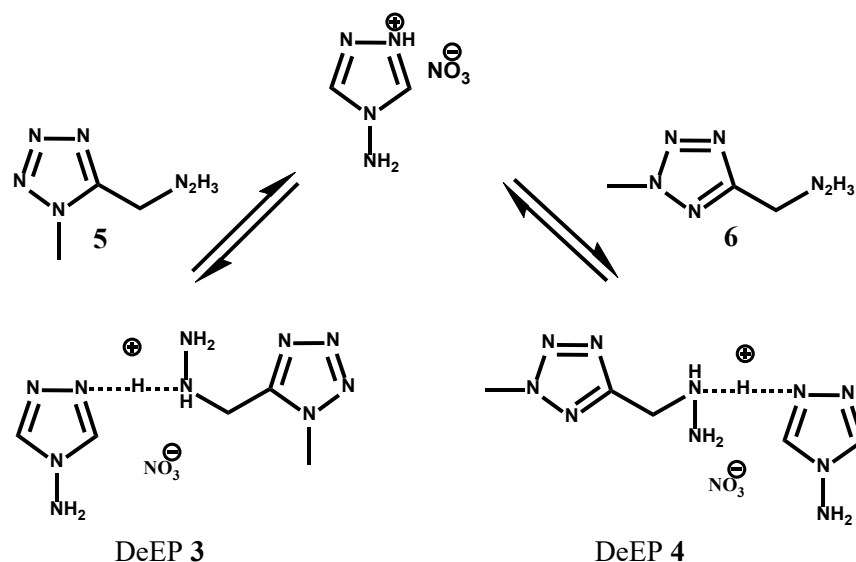

DeEP **2**   DeEP **3**   DeEP **4**

Figure 8. Pictures of DeEP **2 -4.**

Scheme 3. Synthesis of DeEP **1** and DeEP **2** with hydrazine as HBA.

DeEP **1**   DeEP **2**

Scheme 4. Synthesis of DeEP **3** and DeEP **4** with 4ATNO₃ as HBD.

DeEP **3**   DeEP **4**

The melting temperature (T_m) decomposition temperature (T_d) and thermal stability of DeEPs **1-4** and their components were determined using Differential Scanning Calorimetry (DSC) and Thermogravimetric Analysis (TGA) and are listed in Table 2. DSC samples were cooled to -90°C and heated to 250°C at a rate of 10°C /min, TGA samples were heated from ambient to 50°C at a rate of 10°C /min. Figure 9 (left) shows the DSC curve and TGA ramp for DeEPs **1** and **2**. Both, DeEP **1** and **2** reveal no visible melt, DeEP **1** shows a lower T_d than DeEP **2**. The hydrazine containing DeEPs **1** and **2** were further studied by an isothermal TGA to assess their storage stability (75°C held for 24 hours, Figure 9 right) and FTIR. Both DeEP **1** and DeEP **2** exhibit similar trends with a recorded mass loss of 11.9% and 11.4%, respectively.
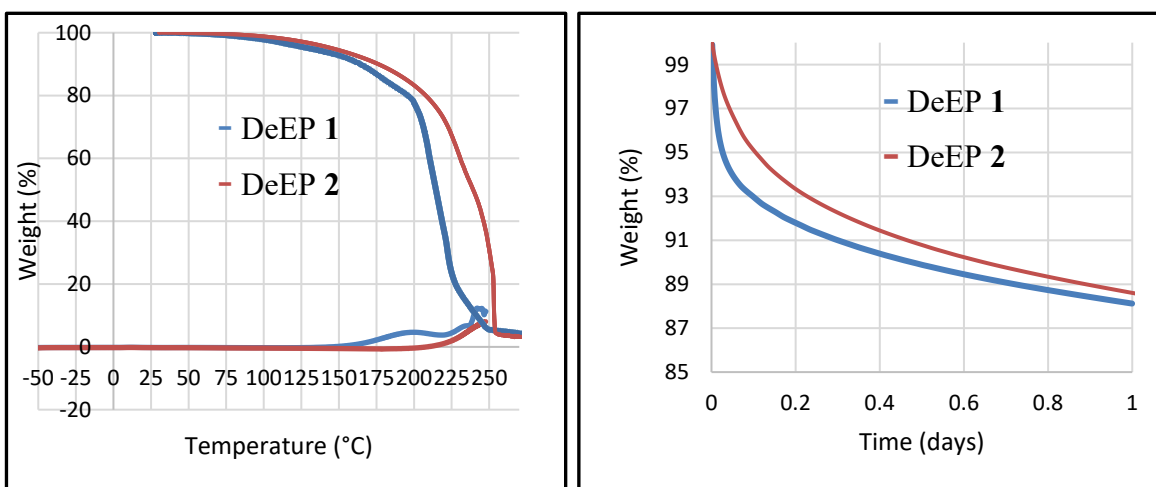
Figure 9. DSC and TGA Ramp of DeEP **1** and **2** (left) and isothermal TGA 75°C 24h (right).

As shown by our previous studies depending on base strength in DeEP **1** and **2** the equilibrium between salts **9** and **10** and hydrazine could completely shift towards the formation of hydrazine nitrate, which would be influencing the evaporative effects observed during isothermal TGA measurements. Hydrazine by itself simply evaporates at 75°C and in a nitrogen stream of 20 l/min used during the TGA experiments (Table 2). If indeed the equilibrium shifts towards hydrazinum nitrate, then the neutral tetrazoles **5** and **6**

12

will still have some volatility according to isothermal TGA data (Table 2), which could explain the recorded mass loss of DeEP **1** and **2**. In case of DeEP **1**, the situation is further complicated by the utilized salt **9** which has a relatively low thermal stability with a T_d of only >100°C. This is also reflected by a mass loss of 8-9wt% observed during an isothermal, 75°C TGA measurement (Table 2), therefore, the mass loss recorded for DeEP **1** could be a combination of evaporation and decomposition of the components present.

However, in the absence of more detailed studies of the TGA residues and or TGA-MS/TGA-IR experiments we assume that the observed mass loss in both cases is due to the loss of hydrazine. The total recorded mass loss for DeEP **1** (11.9%) and DeEP **2** (11.4 %) are very close to each other and the slope of the TGA curve indicates that the end point has not been reached within the 24h measurement period. DeEP **1** and **2** are composed of equimolar amounts of hydrazine and nitrate salt **9** or **10** with mass percentages of 14.3% (hydrazine) and 85.7% (**9** or **10**) respectively. The recorded wt% mass loss in both DeEP is within ~2wt% of the total amount of hydrazine present.

Table 2. Selected physical properties of DeEP **1-4** and their components.

Components	Physical State	T_m (°C)	T_d (°C)	TGA wt% mass loss
N_2H_4	Liquid			100
5	Solid	37	> 175	3-4
6	Liquid		> 175	15-16
9	Liquid		> 100	8-9
10	Solid	103	> 200	3
DeEP **1**	Glass	No melt	> 170	12
DeEP **2**	Liquid	No melt	> 200	11
DeEP **3**	highly viscous	No melt	> 170	
DeEP **4**	Liquid	No melt	> 190	3

FTIR spectroscopy is a suitable tool to study proton transfer processes as the effects of hydrogen bonding within ν_{N-H} stretching region very prominent. Figure 10 shows an overly of FTIR spectra of DeEP **2** and its components, salt **10** and hydrazine. The overlay shows the ν_{N-H} stretching region with pronounced peaks for hydrazine at 3335.7 cm^{-1}, DeEP **2** at 3328.8 cm^{-1}, and **10** at 3229.0 cm^{-1}.
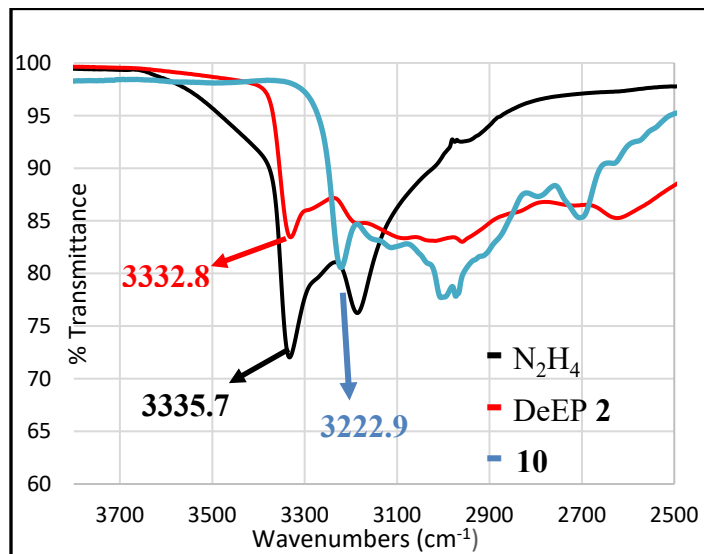

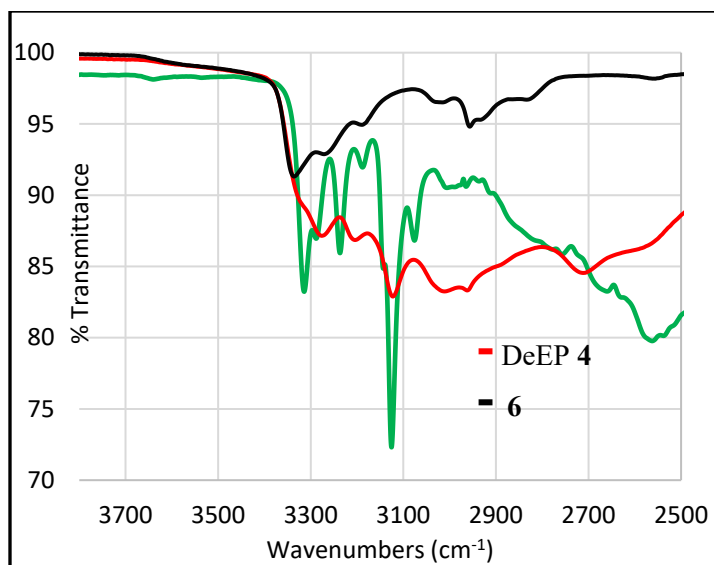**Figure 10**. Overlay FTIR spectra of hydrazine, **10** and DeEP **2**

The FTIR overlay spectra clearly indicate that ν_{N-H} of **10** has disappeared or shifted by more than 100 cm^{-1} to a higher wavenumber in the resulting DeEP **2**, material (from 3222.9 to 3328.8 cm-1), while the ν_{N-H} from hydrazine is only slightly shifted by 3 cm^{-1} to a lower wavenumber in the DeEP mixture. In general, a shift to lower wavenumbers indicates the presence of stronger hydrogen bonding where a shift to higher wavenumbers indicates the opposite effect. Within the DeEP the observed shifts can be interpreted as proton transfer or sharing between **10** (HBD) and hydrazine (HBA). The effect seems to have a larger impact on salt **10** than on the hydrazine molecule. This further supports our assumption that the mass loss in the DeEP material is most likely due to the loss of hydrazine because the hydrogen-bond network is not strong enough to retain the HBA hydrazine at the elevated temperature during the TGA experiment.

The preparation of DeEPs **3** and **4** are shown in Scheme 5. Thermal stabilities of DeEP **3** and **4** were also investigated by DSC. Figure 11 shows the DSC curves of DeEP **3** and DeEP **4** and they exhibit similar thermal stabilities. Since the objective of this research project is focused on liquid DeEP materials and DeEP **3** is a highly viscous almost glass like which renders its unusable for the intended purpose of liquid propellants, only DeEP **4** was subjected to further investigations. Figure 11 shows the overlay of isothermal TGA curves (75°C for 48 hours) of DeEP **4** and its neutral component tetrazole **6**.
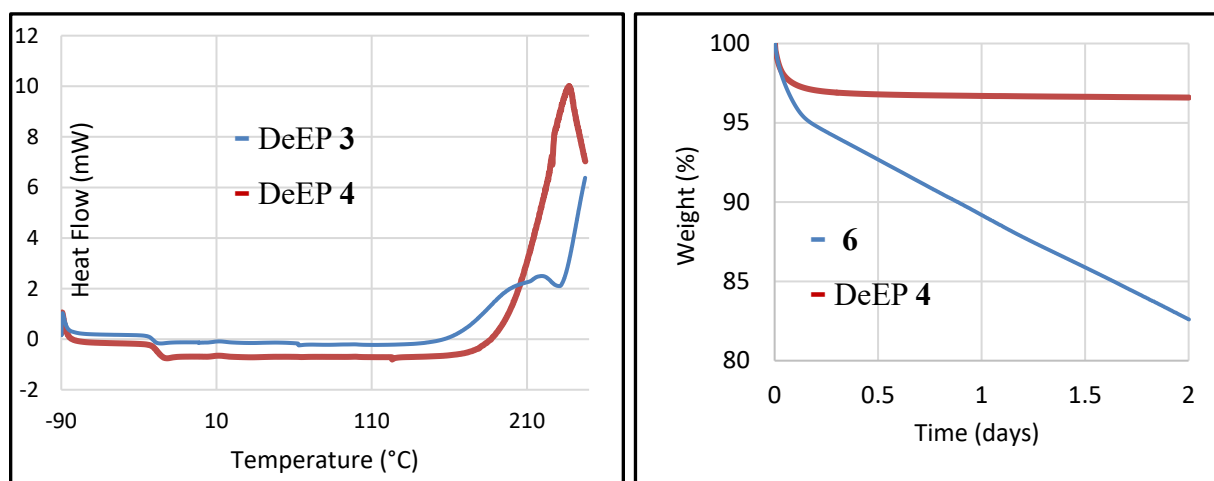

Figure 11. DSCs of DeEP **3** and **4** (left) and isothermal TGA of DeEP **4** and neutral **6** (right)

DeEP **4** is the most thermally stable of all DeEP investigated here with a T_d of >190°C and an only nominal mass loss of 3wt% over a 48h period. As can be seen from the TGA overly of DeEP **4** and its neutral component **6** (Table 2, Figure 11, right), **6** has a considerable volatility as a neutral, unless it would be embedded in a strong hydrogen-bond network. If the acid-base equilibrium within DeEP **4** is such that 4ATNO$_3$ transfers its acidic proton to form the nitrate salt **10** and neutral 4AT, the volatility of **6** would not play a role for DeEP **4** since the overall mixture changed completely. Previous DSC and TGA analysis of nitrate salt **10** showed that it is thermally very stable (Table 2). The strong hydrogen bond interaction or proton transfer was further evident during FTIR studies of DeEP **4**. Figure 12 shows an overlay of the ν_{N-H} region for DeEP **4**, **6**, and 4ATNO$_3$. While it might be difficult to assign the important ν_{N-H} with certainty for the different compounds, a clear trend of signal broadening and a general shift to lower wavenumbers in the ν_{N-H} region can be noted for DeEP **4** if compared to 4ATNO$_3$ and **6**. The line broadening and wavenumber shift are clear indicators for an acidic proton transfer and/or string proton sharing within DeEP **4**.

14

Distribution Statement A: Approved for Public Release; Distribution unlimited. PA# AFRL-2022-5646

Figure 12. Overlay FTIR of DeEP **4**, **6**, and 4ATNO$_3$ in the ν_{N-H} region.

All data presented point to a situation for DeEP **4** best described by Scheme 6. DeEP **4** most likely consists of neutral 4AT and the nitrate salt 10 both of which are solids in their pure state making DeEP **4** a true solid, solid, liquid eutectic.

Scheme 6. DeEP **4** formation

4ATNO$_3$ **6**   4AT   **10**

DeEP **4**
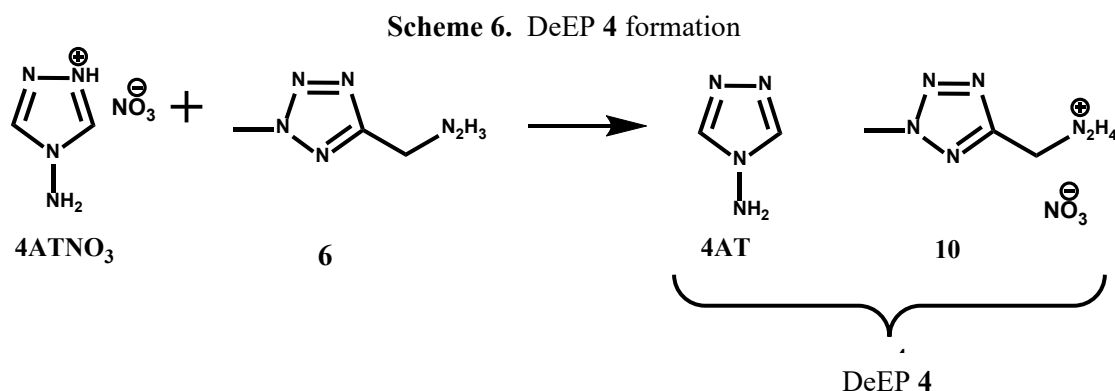
Summary

Several DeEP materials were prepared incorporating high nitrogen tetrazole neutrals and nitrate salts.

The objective of this research is to prepare energetic liquids usable for propellant applications. DeEP **2** and **4** are indeed liquids, while DeEP **1** and DES **3** are glass like materials with insufficient flow characteristics which should be considered a successful *proof of concept* at this stage.

Both TGA and FTIR studies clearly demonstrated that the formation of DeEP **1-4** is accompanied by forming and breaking hydrogen-bonds between the different HBDs and HBAs. In case of DeEP **4**, FTIR and TGA studies point to complete transfer of the acidic proton from 4ATNO$_3$ to the neutral tetrazole **6**, completely changing the constituents of DeEP **4**.

1.4.2 Choline core family of salts

Another part of our DeEP work concentrated on salts containing cations similar to the choline core. The choline cation has been the model cation for most DES work today and other ammonium cation might be equally useful for the formation of DES/DeEP, like the examples shown in Figure 13. We chose to prepare alkylated UDMH salts in which the alkyl group contains either a chloro- or a hydroxyl- group. The salts were evaluated for their potential to form DeEP in conjunction with either urea (a common HBD utilized with choline cations) or 1-AT (a well-established energetic heterocycle and HBD/HBA with good liquifying properties).
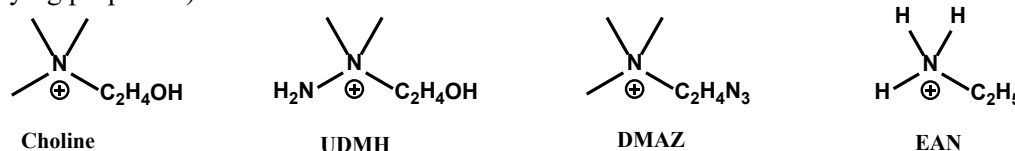
**Figure 13.** Cations with potential for DeEP formation

Synthesis and Characterization

UDMH has been shown to readily react with dichloromethane and 1,2-dichloroethane to form UDMH chloride salts **1** and **2** respectively (Scheme 7). Salts **1** and **2** are good precursors for metathesis reactions where the chloride anions can be replaced with energetic anions such as nitrate, perchlorate, dicyanamide, etc. to generate energetic salts. Their ease of preparation and potential towards energy dense DeEP, prompted us to evaluate their synthesis and physical properties in more detail. Following a literature procedure UDMH was treated with either 2-chloroethanol or 1,2-dichloroethane in refluxing ethanol and crude products were recrystallized from ethanol solutioned layered with diethylether. The chloride salts **2** and **8** are known solids and were characterized by ^{1}H and ^{13}C NMR, FTIR spectroscopy and the structures of **8** was additionally confirmed by single crystal X-ray crystallography (Figure 14). The chloride salt **2** is especially interesting because in addition to the chloride anion, the cation contains a covalently bound chlorine atom which could be replaced with more energetic groups such as hydrazine, azide, or a nitrate ester. Chloride salts **2** and **8** were converted to the corresponding nitrate salts **9** and **10** by metathesis (Scheme 7, 8). Salt **9** is a viscous liquid at room temperature, while **10** is a low melting solid (55.0–58.0°C). Salts **9** and **10** were characterized by ^{1}H and ^{13}C NMR, FTIR spectroscopy and a single crystal X-ray structure was obtained for **10** (Figure 15). Figures 16 and 17 display FTIR over lay spectra of **2** and **10** as well as **8** and **9,** respectively. The FTIR spectra of nitrate salts **9** and **10** clearly show strong absorption peaks at 1336 -1321 cm^{-1}, characteristic for the asymmetric stretching vibration of the nitrate anion, which is absent in the starting materials **2** and **8**.
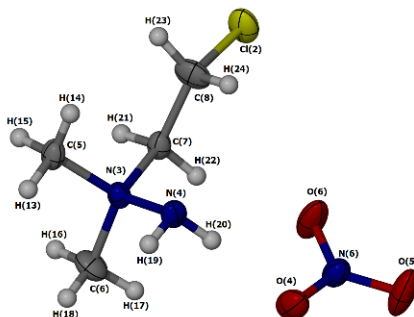
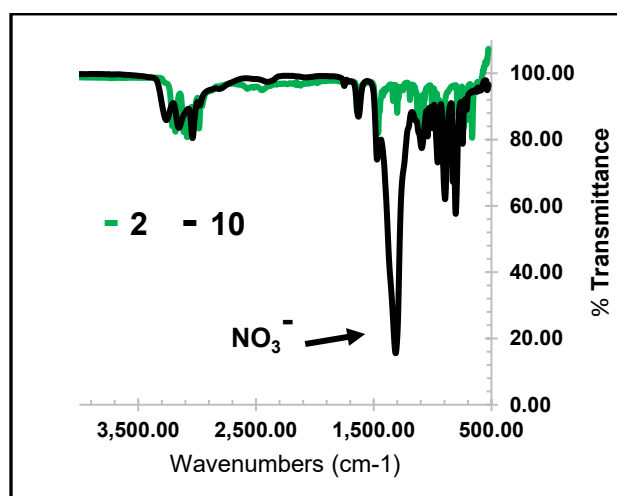**Scheme 7.** Synthesis of substituted UDMH salts.
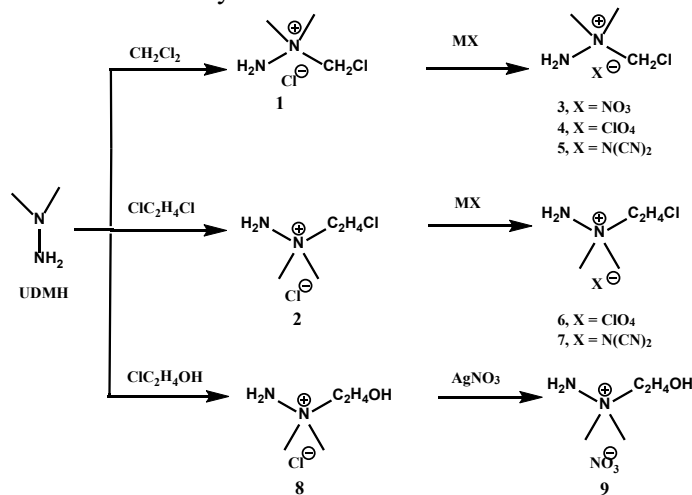
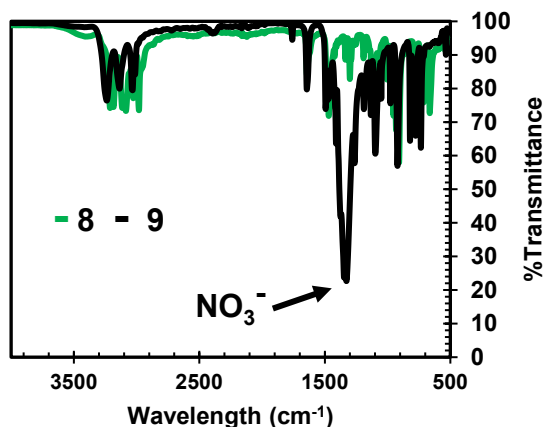**Scheme 8.** Synthesis of nitrate salts **10** and **11**
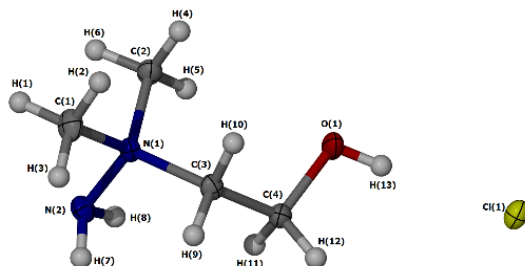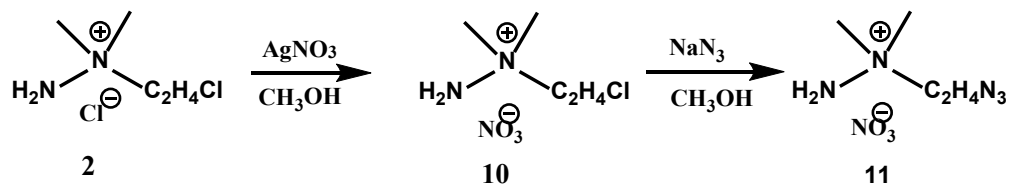
Figure 14. Single crystal X-ray structure of **8**.

**Figure 15.** Single crystal X-ray structure of **10**.

Figure 16. Overlay FTIR spectra of **2** and **10**.

Figure 17. Overlay FTIR spectra of **8** and **9**.

Nucleophilic substitution of halogens by azides is a standard process of introducing azido groups and there are numerous examples of energetic compounds containing covalently bound azido group (C-N$_3$) prepared by this method. The new nitrate salt **10** contains covalently bound chlorine atom (C-Cl) which can be replaced by an azide group (C-N$_3$). Refluxing an ethanolic solution of **10** with a slight excess of sodium azide afforded **11**, which is a viscous liquid at room temperature (Scheme 8). The salt **11** was characterized by ^{1}H and ^{13}C NMR, and FTIR spectroscopy. Both ^{1}H and ^{13}C NMR spectra of **11** showed slight up-field shift for the terminal methylene protons (-CH$_2$N$_3$) compared to **10** (-CH$_2$Cl). The FTIR spectrum of **11** shows the presence of both, the characteristic azido group asymmetric stretching vibration at 2106-2013 cm^{-1} and the asymmetric stretching vibration for the nitrate anion at 1336-1321 cm^{-1} (Figure 18).

Preliminary thermal stabilities of salts **9**, **10** and **11** were investigated using Differential Scanning Calorimetry (DSC). Figure 19 shows an expanded overlay of DSC curves in the region of 120 to 180 °C of **9**, **10** and **11**. Salt **10** has the lowest decomposition temperature onset of about 125-130 °C, while **11** is the most thermally stable of the three salts which is surprising and cannot be easily explained. The decomposition onset temperature of salt **9** lies in between that of **10** and **11** and is greater than 150 °C.
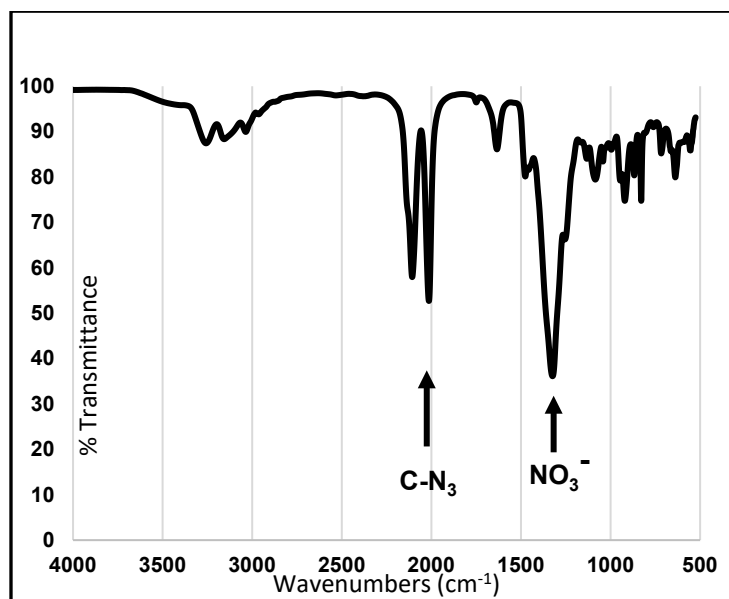
Figure 18. FTIR spectrum of **11**.

18
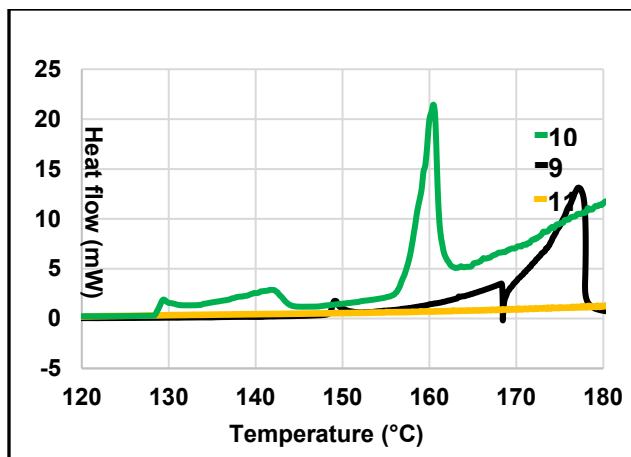
Figure 19. Expanded overlay of DSC curves of **9**, **10** and **11.**

DeEP preparation

As a starting point we selected chloride salts **8** which closely resembles the choline cation as a HBA to combine with Urea (HBD) and the resultant DES/DeEP should confer higher energy than choline chloride and urea. DES/DeEP (**1**–**4**) were prepared by mixing the chloride salt **8** with different molar ratios of urea inside a glove box in a glass vessel and their molar ratios are listed in table 3. The glass vessel was sealed with a septum and the mixture heated to 60 °C for 2 - 6 hours with stirring. The resultant liquids were allowed to cool to room temperature. DES/DeEP **1** and **2** with molar ratios of 1:1 and 1:1.5 of salt **8** and urea are liquids at room temperature. DES/DeEP **3** and **4** with higher molar ratios of urea (1.6 and 2) show the presence of solids in the liquid (Figure 20). Both urea and chloride salt **8** are solids with melting temperature of 133-135 and 160-160° C respectively. Since chloride salt **8** in combination with urea can form liquids, we explored the possibility of other UDMH-core based salts to form DeEP with urea and/or 1-AT, a well-established energetic heterocycle and HBD/HBA with good liquifying properties.

In this regard several DES/DeEP were prepared by combining chloride salt **8** and nitrate salt **9** with either urea or 1-AT at different molar ratios (Table 3). DES/DeEP **5-9** are composed of chloride salt **8** and 1-AT. Except for DES/DeEP **5** (**8**:1-AT, 1:0.5) which is a low melting solid (m.p 40-42 °C) all DES/DeEP are liquids at room temperature with no detectable melting point. DES/DeEP **10-14** are composed of nitrate salt **9** and 1-AT, while DES/DeEP **15–18** are composed of nitrate salt **9** and urea. DES/DeEP **10-12** are liquids, DES/DeEP **13** and **14**, which contain higher molar ratios of 1-AT, are solids with melting points close to room temperature. DES/DeEP **15-18**, prepared from nitrate salt **9** and urea, are low melting solids (24.3–27.4 °C). DES/DeEP **1**–**4** and DES/DeEP **15**–**18** contain urea as the HBD but possess different anions, Cl⁻ or NO$_3$⁻. Comparing all data it appears that the chloride anion causes a larger depression of the melting point. DES/DeEP **10**–**14**, are composed of nitrate salt **9** and 1-AT. Compared to the urea formulations, 1-AT seems to be a better liquifying partner, presumably due to a low melting temperature of 1-AT (49-50 °C). These preliminary results indicate that salts based on a UDMH core cation are viable component for the preparation of energy dense liquid DES/DeEP.

Figure 20. Pictures of DES/DeEP **1-4**

Table 3. DES/DeEP **1 - 18**

Compound	Ratio of component	Physical state	Mp. °C
urea		solid	133-135
1 AT		solid	49-50
8		solid	158-164
9		liquid	No melt
DES/DeEP **1**	**8**: Urea (1: 1)	liquid	No melt
DES/DeEP **2**	**8**: Urea, (1: 1.5)	liquid	No melt
DES/DeEP **3**	**8**: Urea, (1: 1.6)	solid+ liquid	
DES/DeEP **4**	**8**: Urea, (1: 2)	solid+ liquid	
DES/DeEP **5**	**8**: 1AT, (1: 0.5)	solid	40-42.0
DES/DeEP **6**	**8**: 1AT, (1: 1)	liquid	No melt
DES/DeEP **7**	**8**: 1AT, (1: 1.5)	liquid	No melt
DES/DeEP **8**	**8**: 1AT, (1: 2)	liquid	No melt
DES/DeEP **9**	**8**: 1AT, (1: 3)	liquid	No melt
DES/DeEP **10**	**9**: 1AT, (1: 1)	liquid	No melt
DES/DeEP **11**	**9**: 1AT, (1: 2)	liquid	No melt
DES/DeEP **12**	**9**: 1AT, (1: 3)	liquid	No melt
DES/DeEP **13**	**9**: 1AT, (1: 4)	solid	24.3 °C
DES/DeEP **14**	**9**: 1AT, (1: 5)	Solid	28.1 °C
DES/DeEP **15**	**9**: Urea, (1: 1)	solid	25.72 °C
DES/DeEP **16**	**9**: Urea, (1: 1.5)	solid	27.12 °C
DES/DeEP **17**	**9**: Urea, (1: 2)	solid	27.85 °C
DES/DeEP **18**	**9**: Urea, (1: 3)	solid	27.41 °C

Thermal stabilities of DES/DeEP **5-18** were evaluated using Differential scanning calorimetry (DSC). Samples were cooled to - 90 °C and heated to 250 °C, at a rate of 10 °C per minute. The overlay DSC curves are shown in figures 21-23. DES/DeEP **5-9** composed of chloride salt **8** and 1-AT are the most thermally stable DES/DeEP studied so far with decomposition temperature greater than 180 °C (Figure 21). The liquid DES/DeEP **10-12** show similar thermal stabilities, DES/DeEP **13/14** with a higher molar ratios of 1-AT exhibit lower decomposition onset temperatures. The thermal stability of DES/DeEP **10**, composed of 1-AT and nitrate salt **9** was further studied by isothermal TGA, commonly used as a storability screening test. Figure 24 shows the isothermal TGA held at 75°C for 24h for DES/DeEP **10** and its components. Within 24h the nitrate salt **9** loses only 2wt%. In contrast, 1-AT loses about 64wt% mass due to sublimation. DES/DeEP **10**, composed of equimolar ratios of 1-AT and salt **9**, loses approximately 28wt% in the same 24h time period. DES/DeEP **10** consist of 63.5wt% of salt **9** and 33.5wt% of 1-AT. It is assumed that all mass lost is due to 1-AT indicating that hydrogen bonds within DES/DeEP **10** are not strong enough to prevent the loss of the neutral 1-AT component.
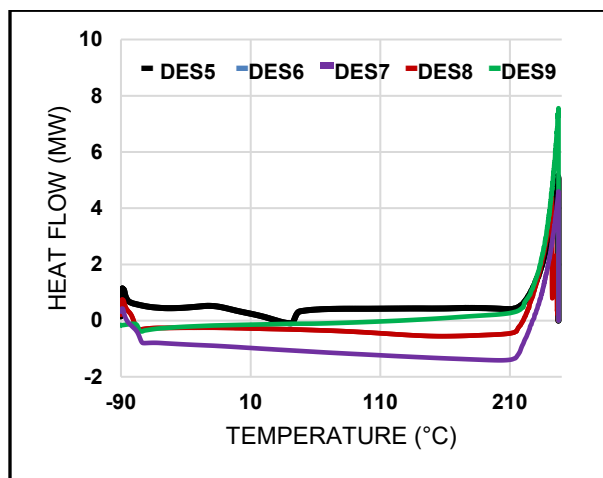
Figure 21. Overlay DSC curves for DES/DeEP **5**–**9**
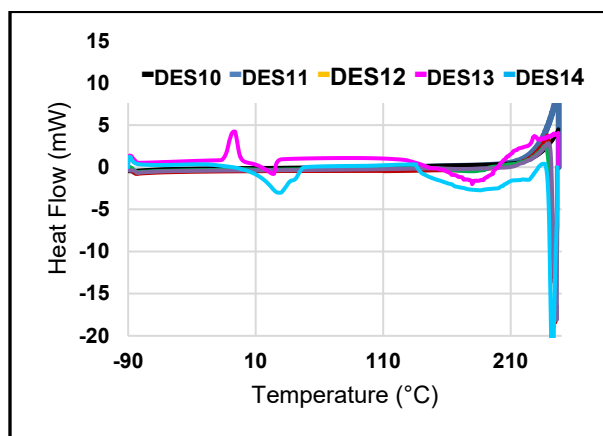
Figure 22. Overlay DSC curves for DESs **10-14**
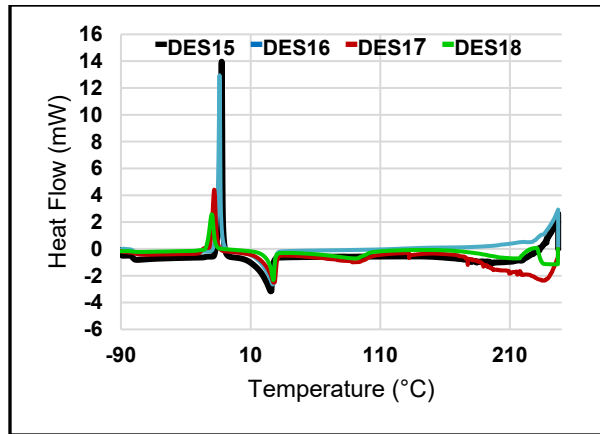
Figure 23. Overlay DSC curves for DES/DeEP **15**-1**8**
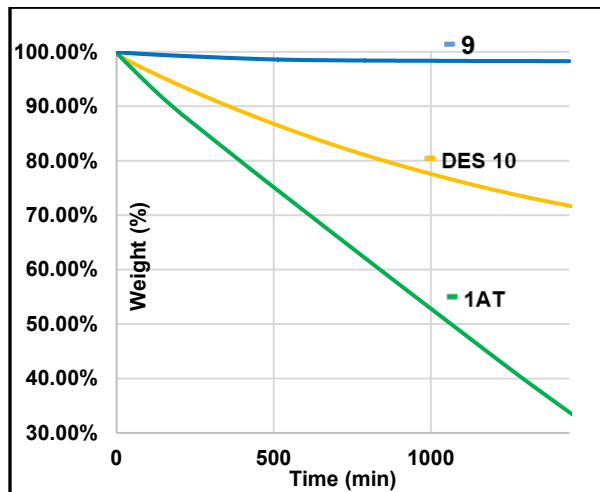
Figure 24. Overlay of isothermal TGA of 1-AT, **9** and DES/DeEP **10** held at 75°C for 24 hours

Summary

The accumulated data presented here clearly indicate that HBA/HBD interactions between energetic salts based on a UDMH core and 1-AT or urea are real, making these salts viable candidates to generate energy dense liquid DES/DeEP. In the future initial hazard properties of these DES/DeEP need to be investigated to assure that they are safe to use. Our past experience showed an increased sensitivity of some initially evaluated DES/DeEP formulations compared to their components. If these new DES/DeEP materials show improved safety properties, methods to successfully ignited them need to be studied in detail to render them useful for potential propellant applications.

1.5 Task I Results: Solvated Ionic Liquids

1.5.1 Chemistry in solution

The chemistry of lithium molecules containing cyanoborohydride anions (or an extended cyanoborohydride framework motif) have barely been researched. Though the base molecule, lithium cyanoborohydride, was synthesized over 65 years ago, there has yet to be a crystal structure determination of the compound published. Further, there is only one known lithium salt in the literature of the higher homologues of cyanoborohydride reported (Figure 25). Due to the electron withdrawing nature of the cyano moiety, the reducing strength of the anion is lowered over a similar borohydride. This property makes the anions ideal for further exploration of the coordination chemistry of the proposed, high nitrogen ligands (Figure 25). Further, given the unsymmetrical nature of the proposed anionic species, issues regarding rotational disorder within the anion will be minimized, allowing us to better characterize the materials via x-ray crystallography.

Our primary research interests in the production of SILs and the propensity of cyanoborohydrides to produce liquids enhanced our drive to investigate these compounds. We have reported our ability to produce room temperature SILs based upon $LiBH_4$ using small, low boiling amines, so the incorporation of the extended cyanoborohydride motif should allow for the promotion of other liquids. Our focus will be on utilizing high energy, especially high nitrogen containing, ligands to improve the overall performance of the resulting compound in combination with the varied anionic species. This will not only greatly improve the knowledge of the coordination chemistry of the anionic species but offers the potential of turning these materials into high energy liquids.
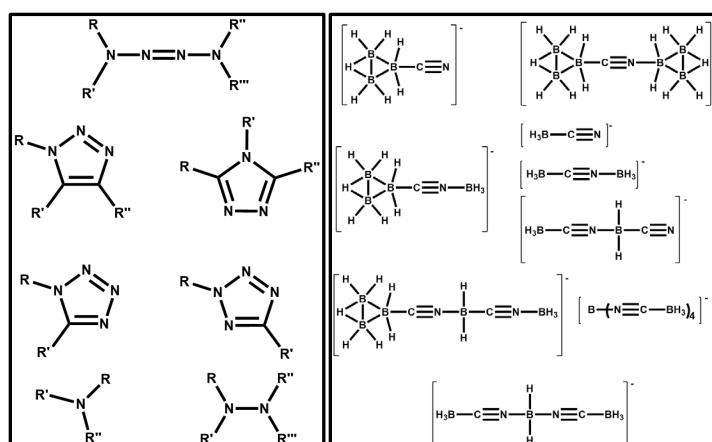
Figure 25. Proposed ligands and anionic species to be investigated

First, we concentrated on the synthesis of the simplest proposed compound, lithium cyanoborohydride ($LiCNBH_3$). This was successfully accomplished by the metathesis of commercially available sodium cyanoborohydride ($NaCNBH_3$) with lithium chloride (LiCl) in tetrahydrofuran (THF) with a near quantitative yield of high purity material. Unlike previous attempts to make lithium salts of borohydrides, the THF was easily removed by heating the solid to 90°C under vacuum, leaving the uncoordinated salt for further chemistry. According to the ^1H spectra (Figure 26a)) where the anticipated multiplets representing THF (peaks at ~1.8 and 3.7 ppm) the final product show an approximately 1% contamination by THF.
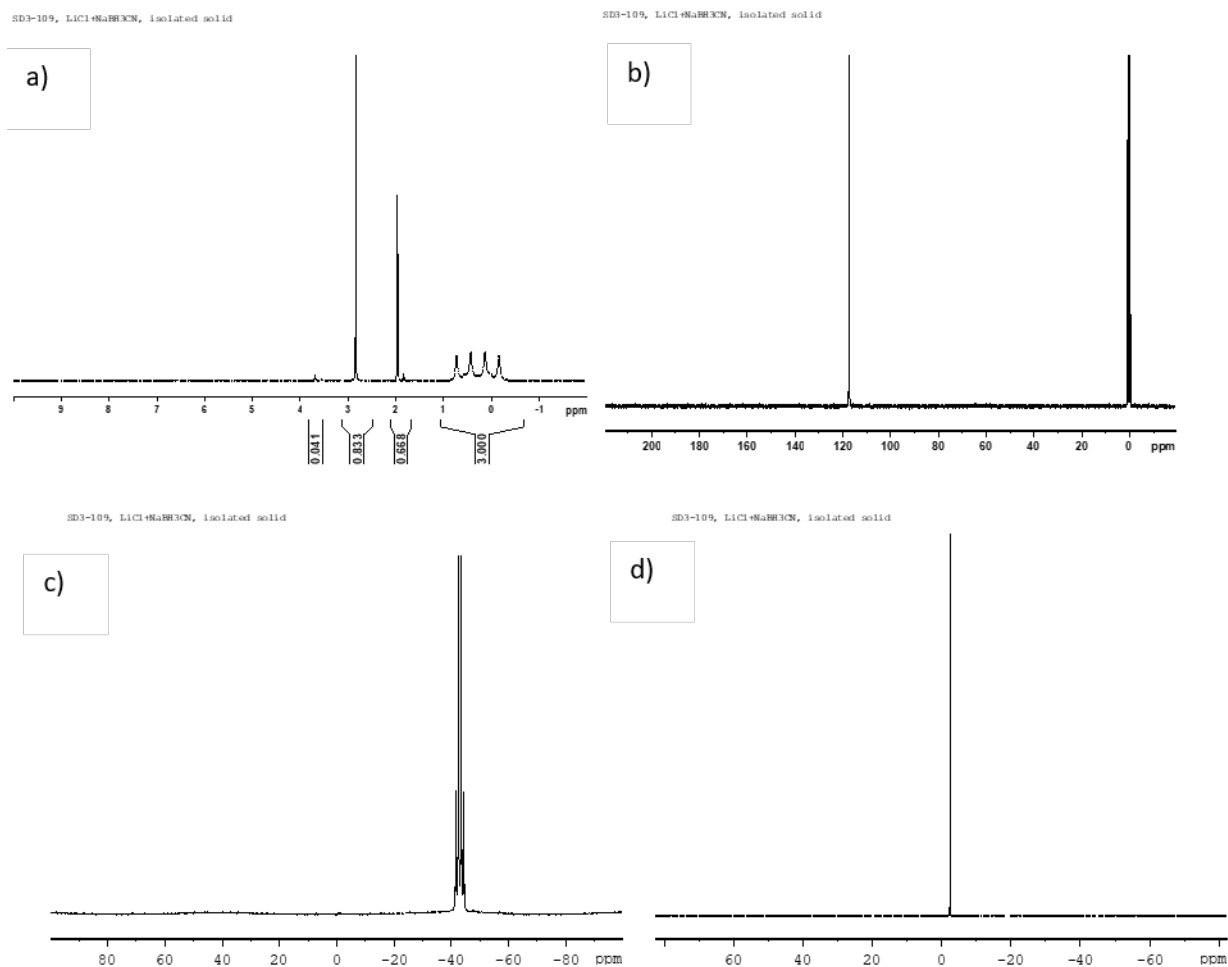
Figure 26. NMR Spectra of LiCNBH$_3$: a) ^{1}H b)^{13}C c)^{11}B d)^{7}Li

After we demonstrated that the materials can be obtained solvent free, attempts to coordinate simple amines to the Li cation were undertaken. The first compound chosen, due to its potential performance payoffs was monomethylhydrazine (MMH). The synthesis was performed using two equivalents of MMH per lithium cation and the reaction resulted in a viscous oil. The ^{1}H NMR shows a 2:1 coordination (Figure 27a)), which was anticipated due to the stoichiometry of the reaction. Upon drying the compound in a dynamic vacuum for one hour, it was noted that the ratio of ligand to borohydride decreased, based on the integration of the ^{1}H NMR (Figure 28a)). Finally, when drying the compound for 10 hours, a white solid was formed. The ^{1}H NMR (Figure 28b)) shows that the final ligand ratio fell to 1.5:1.

This phenomenon was also observed when coordinating hydrazine to LiCNBH$_3$, Figure 29a) and Figure 30 a,b).
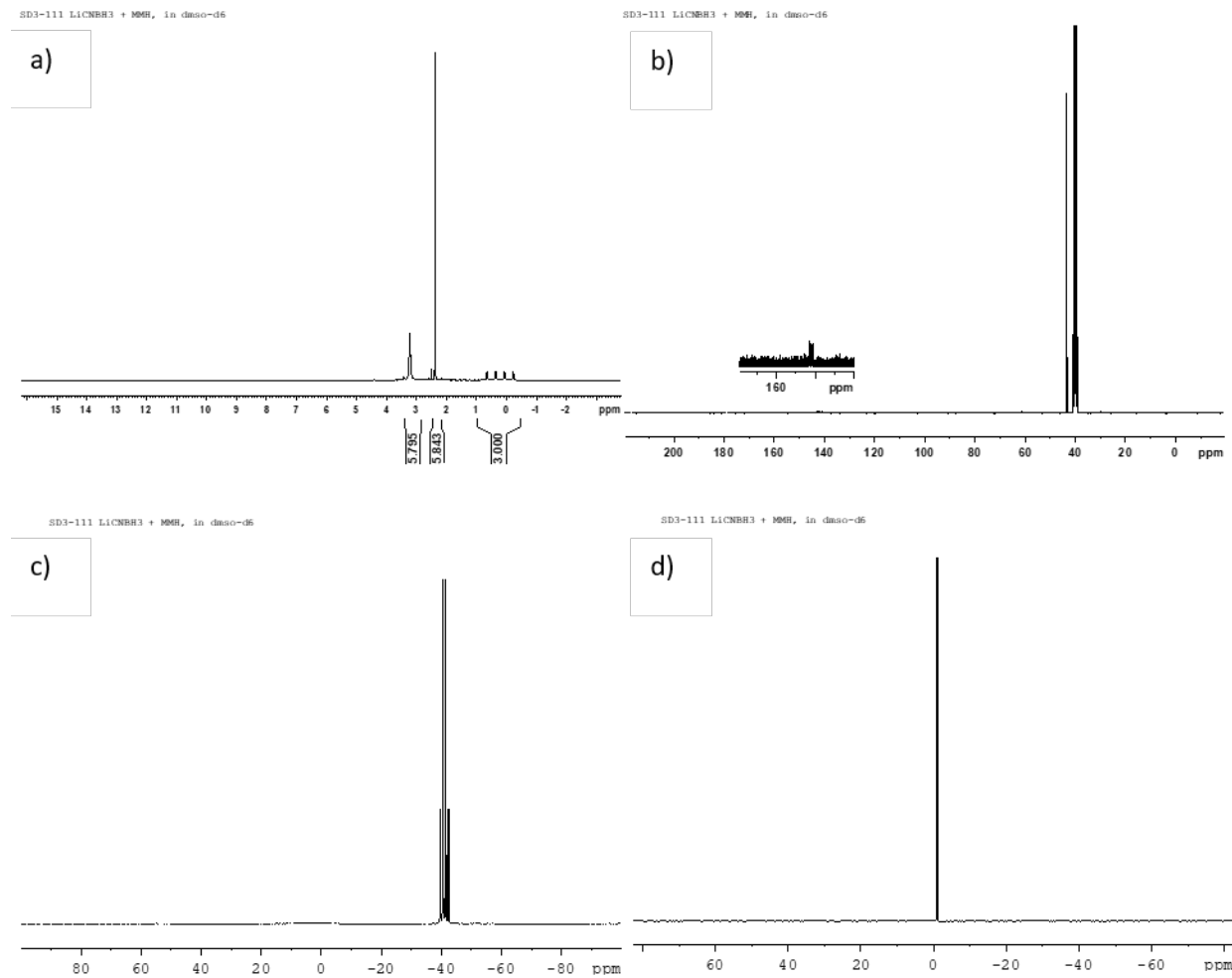
Figure 27. NMR Spectra of Li(MMH)$_2$CNBH$_3$: a)^{1}H b)^{13}C c)^{11}B d)^{7}Li
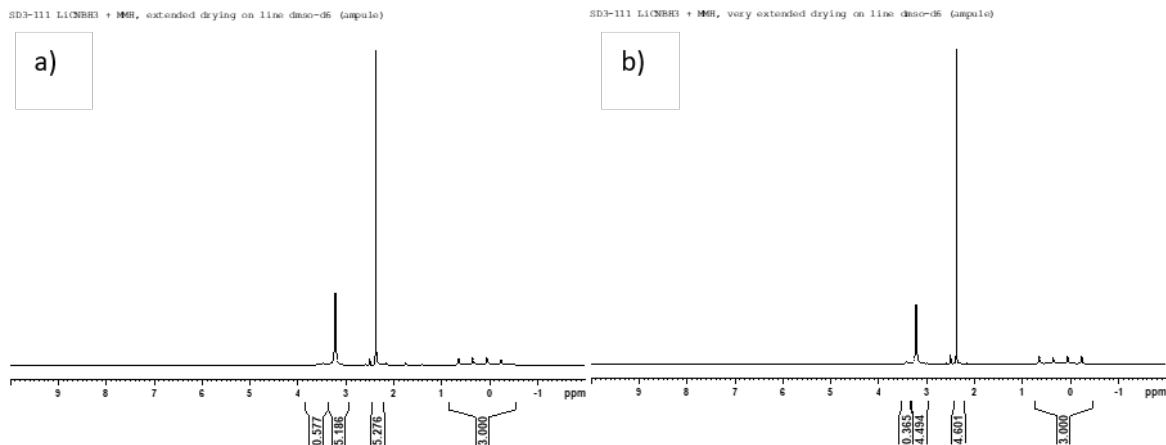
Figure 28. ^{1}H NMR Spectra of Li(MMH)$_2$CNBH$_3$ after drying: a)1 hour b)overnight

25
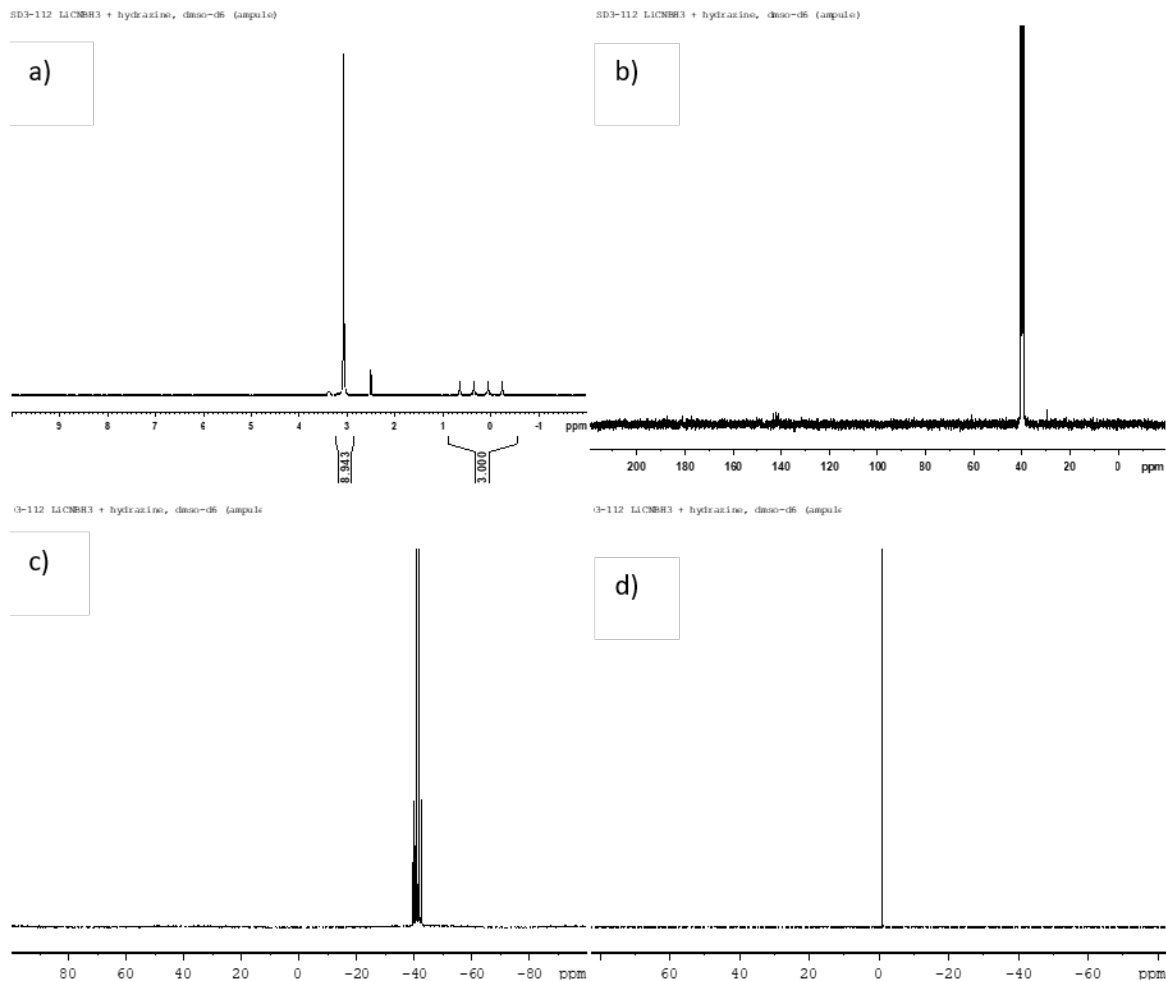
Figure 29. NMR Spectra of Li(hydrazine)$_2$CNBH$_3$: a)^{1}H b)^{13}C c)^{11}B d)^{7}Li
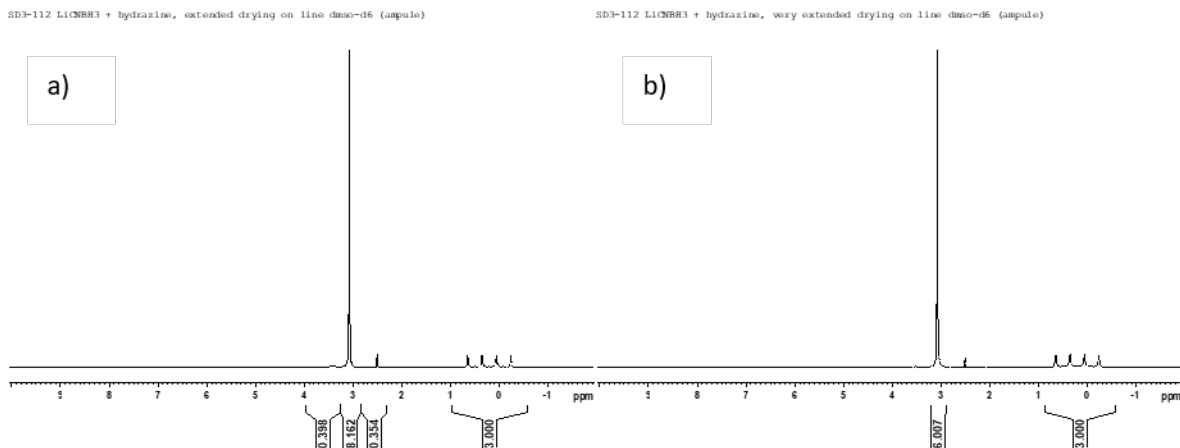
Figure 30. ^{1}H NMR Spectra of Li(hydrazine)$_2$CNBH$_3$ after drying: a)1 hour b)overnight

The ability of the LiBH$_3$CN to form stable coordination compounds with the hydrazines, prompted us to look into the coordination of some other simple amines like ammonia, methylamine, dimethylamine,

26

ethylamine and dimethylisopropylamine. The reactions were carried out in the absence of any solvent, condensing the neat amines onto lithium cyanoborohydride at liquid nitrogen temperatures. Unfortunately, none of the amines formed as strong a coordination as the hydrazine derivatives. As a representative example, the NMR investigations with ammonia are shown in Figure 31. At first, when the ammonia is in excess Figure 31b), the amine ligand to lithium ratio appears to be 4:1, while after allowing all excess ammonia to boil off, the ligand ratio drops to 3:1, Figure 31a). During pumping in a dynamic vacuum (Figure 31c) and d)), the amount of the coordinated amine continuously drops, and after 8 hours reached a ratio of only ~0.5:1. Furthermore, the consistence of the residue was of a tacky, semi solid, indicating that the reminder of the amine could be completely removed upon further pumping. This also demonstrates the completely dynamic/reversible nature of these coordinating amine ligands, obviously
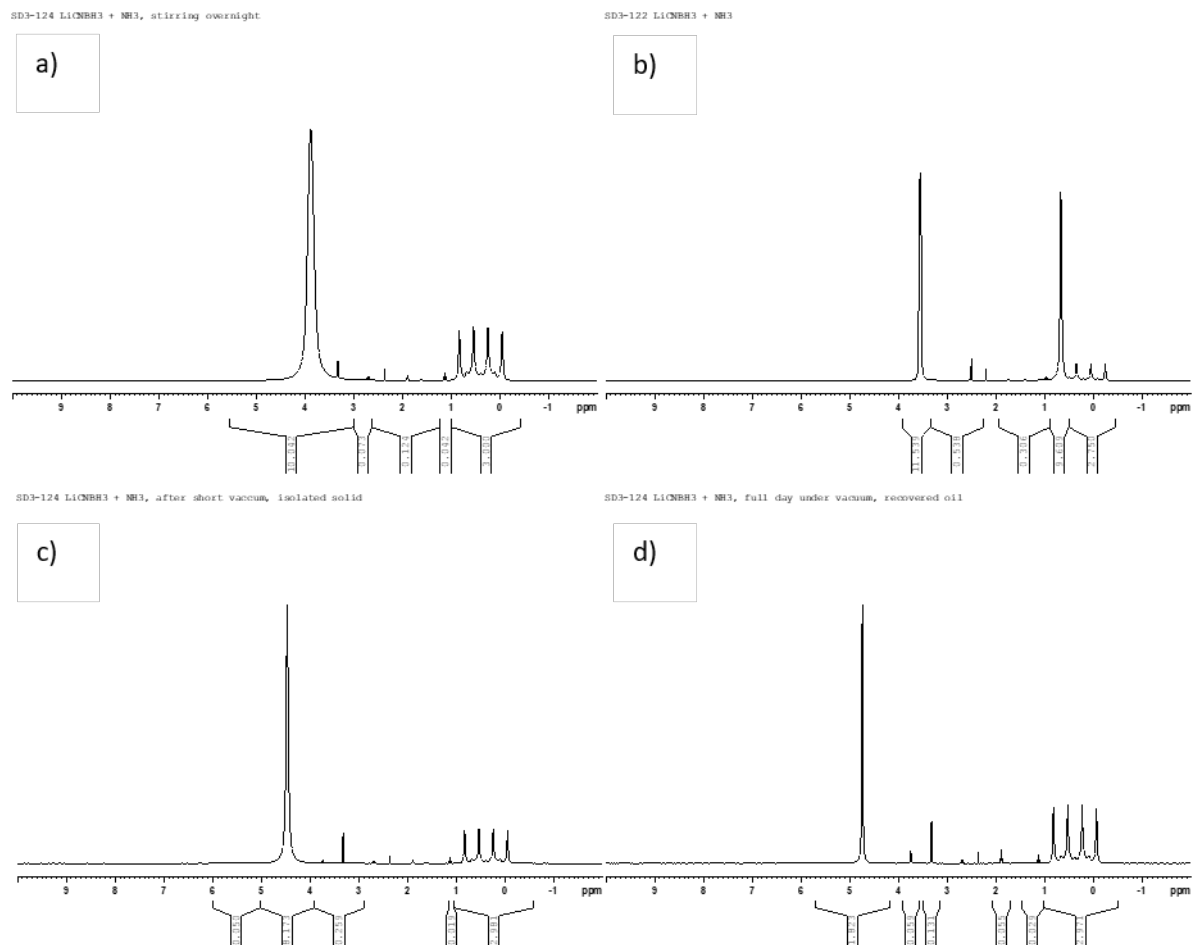
Figure 31. ^{1}H NMR Spectra of Li(NH3)$_x$CNBH$_3$: a)Stoichiometric Ammonia b) Excess Ammonia c) 15 minutes of vacuum d) 8 hours of vacuum

being able to form loose coordination compounds at well-defined ratios which easily de-coordinate depending on the conditions.

As it was outlined in our proposal the addition of $LiCNBH_3$ to state-of-the-art propellants like the hydrazines shows no advantageous performance improvement. This changes when moving to more complex anionic species like $[B_3H_7CNBH_3]^-$. Following a literature procedure published by Morris, et. al., the tetrabutylammonium salt of $[B_3H_7CNBH_3]^-$ was readily synthesized. Initial efforts were to replace the bulky cation with sodium. It was anticipated that a metathesis reaction using sodium tetraphenylborate ($Na[B(C_6H_5)_4]$) should lead to the clean formation of tetrabutyl-ammonium tetraphenylborate and the desired sodium salt. However, all our endeavors so far, yielded a material still contaminated with both tetrabutylammonium and tetraphenylborate, even after washing with copious
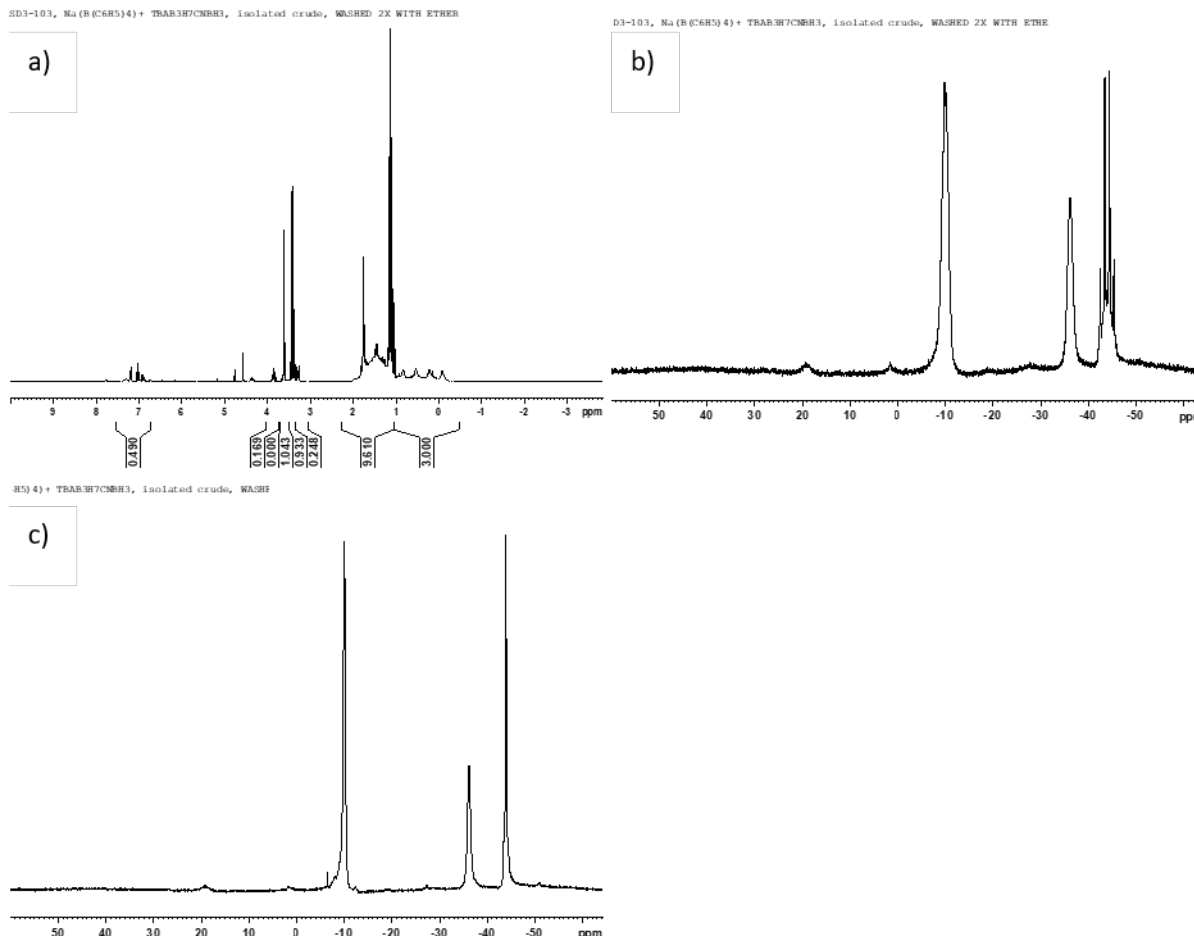
Figure 32. NMR Spectra of $NaBH_3CNB_3H_7$: a)^{1}H b)^{11}B coupled c) ^{11}B decoupled

amounts of diethyl ether (Figure 32). This challenge is still being addressed and other methods of producing the sodium salt are under consideration.

Another anion of interest is $[BH_3CNBH_2CN]^-$. The synthesis of the sodium salt has been mentioned twice in the literature, however, in both cases the sodium is not "free" but coordinated by 1,4-dioxane. Given the thermal stability of the cyanoborohydride anion, it was anticipated that the solvent could be removed by vacuum and heat. Unfortunately, all our efforts resulted in the decomposition of the anion rather than the de-coordination of the 1,4-dioxane. Other synthesis routes to obtain an uncoordinated sodium salt are being explored.

A third anionic species pursuit during this year was $[BH_3CNBH_3]^-$. Again, the sodium salt of this anion had been previously synthesized. During our experiments it was observed that an equilibrium is formed between the $[CNBH_3]^-$ and $[BH_3CNBH_3]^-$. This is clearly shown by the integration of the signals in the ^{11}B spectrums (Figure 33a) and b)).

In Figure 33a), the excess THF-BH$_3$ used during the reaction appears as a quartet at approximately 0 ppm. The integration of the two other quartets, associated with the two magnetically inequivalent BH$_3$ groups, are at the expected 1:1 ratio. However, once the solvent (and excess is THF-BH$_3$) is removed and a solid is isolated, the integration of the two peaks is no longer equal in intensity and an underlying boron signal associated with [CNBH$_3$]$^-$ is visible. The intensities of the initial quartet at -44 ppm became distorted and a decoupled spectrum clearly showed two peaks in this region (not shown). Since these two anions are not easily separated the synthesis of [BH$_3$CNBH$_3$]$^-$ has been put on hold.
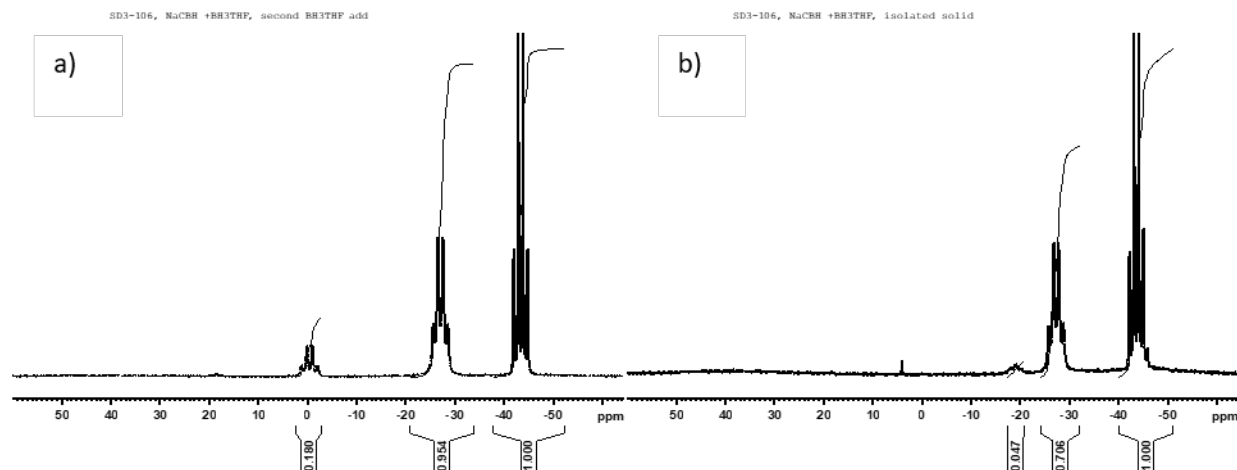
Figure 33. ^{11}B NMR Spectra of NaBH$_3$CNBH$_3$: a) THF-BH$_3$ in excess b) isolated solid

Summary

It was demonstrated that amine ligands coordinate with the lithium cation in LiBH$_3$CN. However, the coordination strength must be considered as overall weak. In general, the amine ligands can be removed from the lithium salts under relatively mild conditions. In the case of hydrazine and monomethyl-hydrazine a well-defined ligand to lithium ratio was established but the resulting materials are solids which is undesirable. It remains to be seen what impact hydrazine and/or amine solutions of LiBH$_3$CN have on the overall vapor pressure of the resulting mixture which still might them render as useful energetic liquids.

The ionic species explored, outside of the simple cyanoborohydride, had various issues, typically discovered during the isolation of the desired pure salts. It must be concluded that pure salts will be extremely difficult to make in quantity, considering that the best solvents available are strongly coordinating with the metal cation and that various anions are in different equilibria with each other in solution.

1.5.2 Mechanochemical approach

A solvent free, mechanochemical synthesis approach as a method to prepare various borohydride anions, which could offer the advantage of circumventing the problems discovered during solution chemistry was pursued. It could also be considered an environmentally friendly, "greener" approach since it is solvent free.

The most complete description of the milling process to produce simple sodium amidoborane according to equation **1** was described in a paper by Milanovic and Biliskov. In the process, pre-milling of aminoborane was required to allow for better blending with the sodium hydride. In the procedure, there is no noted milling speed, but their varied times showed that there is the potential to decompose the product during the milling process, due to the extended time and energy put into the system.

$$NaH + NH_3BH_3 \longrightarrow NaNH_2BH_3 + H_2 \quad (1)$$
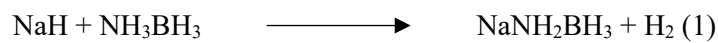
Further, it has been seen that trace contaminants of iron may affect the decomposition of some boranes, therefore, a milling system constructed of zirconium oxide is being utilized in the current research (balls and jar lining). Due to the differences in density of milling with ZrO_2, the density of ZrO_2 is 5.68 g/cm^3 versus stainless steels (the most common system in the literature) value of ~7.8 g/cm^3, new protocols for the synthesis of the boranes are required. As a general statement, the milling process, as seen in the literature details the amount of time milled with very little emphasis on speed (RPM).

The initial investigation of the reaction was stalled due to the late discovery that the milled materials were reacting with the utilized NMR solvents tetrahydrofuran (THF) and acetonitrile (ACN), resulting in NMR spectra where the purity of the final material could not be effectively evaluated. These reactions caused multiple peaks to appear in the ^{11}B NMR falsely indicating that multiple products were produced during the milling process (Figure 34). After screening multiple solvents, dimethylsulfoxide was found to be a suitable NMR solvent for our investigations.
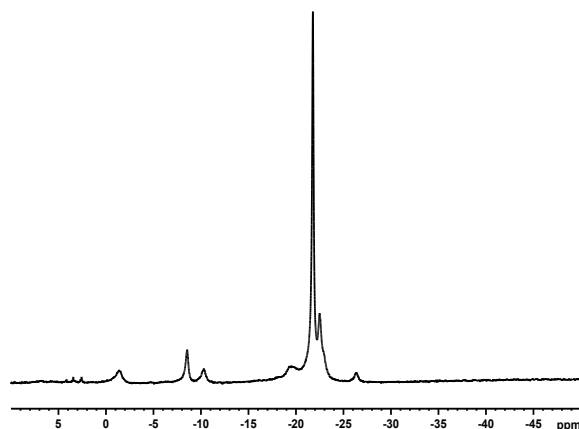
Figure 34. ^{11}B-^{1}H Decoupled NMR of Milled Product in THF-D8

With the ability to track changes successfully by NMR, the following general conditions were chosen. All reactions were performed on a 20 mmol scale giving a combined mass of the reactants equal to 1.1 g and the combined mass of the zirconium oxide milling balls to as close to 75 g as possible (10 mm = 75.44 g, 15 mm = 74.00 g and 20 mm = 75.14 g).

The milling speed (200-325 RPM) was varied between each reaction to determine the optimum speed for each milling ball size. After a set period of time, the milling jar was transferred into a glovebox where an NMR sample was taken under a nitrogen atmosphere. If the reaction was incomplete, as determined by the ^{11}B NMR spectroscopy, more milling was performed. If the reaction was complete, the material was collected, and a yield determined. For samples that showed decomposition, the reaction was discarded. The resulting data are listed in Table 4.

Table 4. Reaction Data for NaH + NH$_3$BH$_3$ at Different Milling Speeds (RPM)

Rxn #	RPM	Ball Size	Yield g	Yield %	Run Program	^{11}B-^{1}H Decoupled Peaks (Integration)	Solid Color
18	200	15 mm			1hr+1hr+30 Min	-21.9 (1.0)	White
			1.001	92.69	1hr+1hr+30 Min	-19.5(1.0)	White
19	200	10 mm			1hr+1hr+30 Min	-19.1(1.0)	Purple
			0.67	62.04	1hr+1hr+30 Min	-19.5(1.0)	White
20	200	20 mm	0.756	70.00	1hr+1hr+30 Min	-19.3(1.0)	Purple
21	250	15mm			1hr+1hr+30 Min	-19.0(1.0), -20.5(0.22), -35.5(0.05)	Purple
					+ 1 hr	-19.0(1.0), -20.5(0.18), -35.5(0.04)	Purple
			0	0.00	1hr+1hr+30 Min	-19.0(1.0), -20.5(1.49), -35.5(0.14)	Purple
22	250	10mm	0	0.00	1hr+1hr+30 Min	-19.0(1.0), -20.75(1.15), -35.5(0.22)	Purple
23	250	20mm	0	0.00	1hr+1hr+30 Min	-16.05(0.13),-18.29(0.42),-19.0(1.0), -20.75(2.01), -35.5(0.64)	Purple
24	225	15 mm	0.965	89.35	1hr+1hr+30 Min	-19.1(1)	White
25	225	10 mm			1hr+1hr+30 Min	-19.1(1)	Purple
			0.661	61.20	+1 hr+1hr	-19.1(1), -20.86(0.03)	light purple
26	225	20 mm	0.897	83.06	1hr+1hr+30 Min	-19.5(1)	White
27	250	15 mm			+ 1 hr	-19.5(1)	Purple
			0.606	56.11	+ 1 hr	-19.3(1), -20.7(0.03), -35.8(0.02)	light blue
28	225	10 mm			1hr+1hr+30 Min	-19.1(1)	Purple
					+ 1 hr	-19.1(1), -20.6(0.02)	Purple
					+ 1 hr	-19.1(1), -20.6(0.02)	Purple
			0	0.00	+ 1 hr	-19.1(1), -20.6(0.06)	Purple
29	250	15 mm	0.877	81.20	45 min +45 Min	-19.1(1)	White
30	250	10 mm	0.822	76.11	45 min +45 Min	-19.1(1)	Purple
31	250	20 mm	0.535	49.54	45 min +45 Min	-19.1(1)	Purple
32	275	15mm	0.927	85.83	30 min + 30 min	-19.1(1)	White
33	275	10 mm	0	0.00	30 min + 30 min	-20.6(1),-23.5(0.03), -35,6(0.01)	Purple
34	275	20mm	0	0.00	30 min + 30 min	-19.1(1), -20.6(0.16), -35.6 (0.02)	light blue
35	275	10mm	0	0.00	20 min + 20 min	-19.1(1), -20.7(0.07),-35.7(0.04)	Purple
36	300	15mm	0.825	76.39	20 min + 20 min	-19.1(1)	White
37	300	10 mm	0	0.00	20 min + 20 min	-15.9(0.16),-19.2(1),-20.5(0.54),-35.6(0.25)	Purple
38	300	20mm	0	0.00	20 min + 20 min	-16.1(0.16),19.1(1),-20.5(0.54),-35.6(0.26)	Black
39	300	10mm	0	0.00	10 min	-3.9(0.03),-8.4(0.07),-18.2(0.08),-19.3(1),-20.6(0.08),-21-2(0.14),-22.9(0.09),-35.7(0.13)	White
40	325	15mm	0	0.00	10 min+10 min	-16.1(0.36),-18.2(0.08),-19.3(1),-20.6(0.08),-21.2(0.14),-22.9(0.09),-35.7(0.13)	Purple
41	300	15 mm			2x20 min	-22.9(1)	White
			0.793	73.43	+20 min	-19.5(1)	White
42 (half scale)	250	15mm	0	0.00	2 x 45 min	-18.3(0.15), -19.1(1), -20.6(1.54), -35.6(1.57)	White
43 (2xscale)	250	15 mm			2 x 45 min	-19.6(1)	White
			1.897	87.82	+45 min	-19.5(1)	White

The initial experiment at 200 RPM (using 15mm milling balls) showed that at this speed the reaction would not go to completion during the first milling cycle (Figure 8, 2nd curve, -22.0 ppm). This can be clearly seen by the shift of ~1 ppm in the ^{11}B NMR compared to the starting material, NH$_3$BH$_3$ (Figure 35, 3rd curve, -22.9 ppm) with a minimal narrowing of the peak width. After a second milling cycle, a further
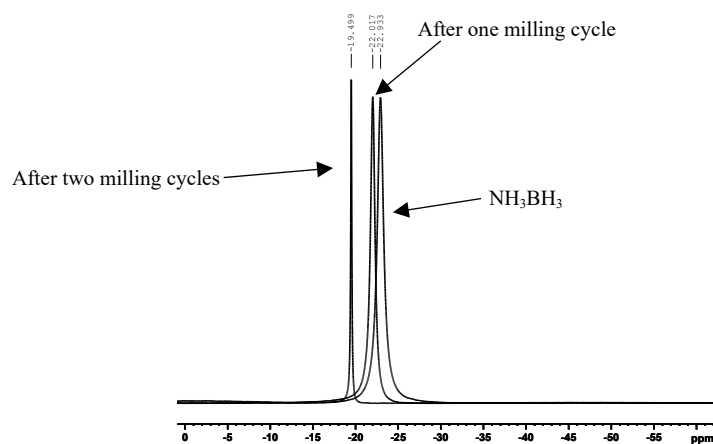
Figure 35. ^{11}B-^{1}H Decoupled NMR Spectra Overlay for Reaction #18

shift in the spectrum is observed to -19.5 ppm (Figure 35, 1st curve), together with a noticeable narrowing of the peak width, which suggests a notable change from the neutral aminoborane during the milling process.

Interestingly, in the milling process at 200rpm with the 10mm milling balls the material in the jar was purple in color after the first cycle (Table 4, Rxn #19). This was reminiscent of the material described by Milanovic, et al. when no pre-milling of the aminoborane was performed. Further, the ^{11}B NMR shows an even larger shift than previous observed down to -19.1ppm. Due to the purple color, another milling cycle was performed to determine whether the reaction was complete. After this cycle, the color of the solid changed from purple to white, and the ^{11}B NMR peak shifted back to -19.5ppm with a slight peak broadening. The change in color, in combination with the spectral change strongly suggests formation of an intermediate during the reaction that is not traceable by NMR. This aspect was not investigated in

31

further detail, though it could be an interesting subject for a modelling and simulation effort of the reaction pathway.

The final effort at 200rpm, with the 20mm milling balls, again showed a purple product, with the ^{11}B NMR shift at -19.3ppm. Since the material formed appeared to be following the same path as noted with the 10mm milling balls, experiments moved to higher rpm.

The same procedure was used at 250rpm, and at this speed, it appears the material starts to decompose during the first milling cycle (Table 4, Rxn #21). This is seen by the formation of new peaks at -20.6 and –35.6ppm in the ^{11}B NMR (Figure 36a). It is reasonable to presume that the peak at -35.6ppm corresponds to the formation of $NaBH_4$, due to the associated quintet in the coupled spectrum. The broad peak at -20.6ppm is an unknown at this point and might be investigated later. Not surprisingly, when the reaction mixture is milled for a longer period of time, the amounts of the decomposition products grow. The same decomposition products are also identified in the reactions carried out with the 10 and 20mm milling balls, though in the case of the 20mm milling balls, there are even more decomposition products present according to the ^{11}B NMR spectra (Table 4, Rxn #23) suggesting that the larger ball size delivers more overall energy. All reactions in this set resulted in solid products with a purple color. This may infer that one of the decomposition products is also colored, making it difficult to decide if the solids simply need to be milled longer, just based on color.

Due to the obvious formation of decomposition products at 250rpm, the milling speed was reduced to 225rpm and the milling protocol was repeated (Table 4, Rxn #24-26).
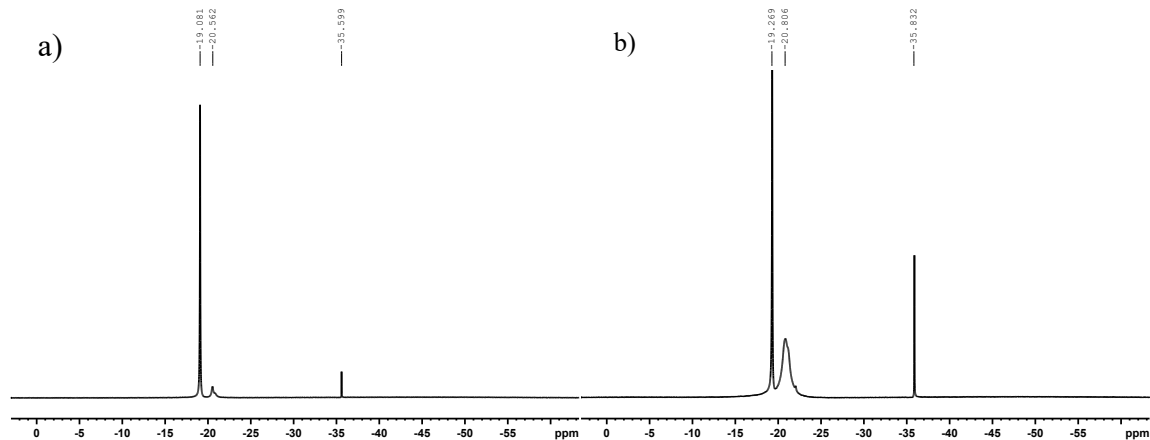
Figure 36. ^{11}B NMR of Reaction #21   a) after first milling cycle   b) after second milling cycle plus one hour

Under these conditions, the 15mm milling balls produced a white product, though the ^{11}B NMR shift is at -19.1ppm. For the 10mm milling balls, the product again was purple and the signal in the ^{11}B NMR is identical the previous experiment with the 15mm milling balls. To see whether the color of the material might change upon further milling, the reaction mixture was milled again for a total of 2h. The materials color changed, but it was still a faint purple color. The ^{11}B NMR spectra clearly showed that decomposition products start to form, with a small peak appearing at -20.6ppm.

The experiment with the 10mm milling balls was repeated (Table 4, Rxn #28), delivering the same result which was obtained after the first cycle of the previous attempt. Milling was continued for 1h and the material was re-inspected. Still, the material had a purple color, and the formation of decomposition products was visible in the ^{11}B NMR. In order to gauge how quickly decomposition products are formed and color change might occur, the milling was continued two more times for an additional hour each run,

and the resulting material was investigated after each run. There was no discernable change in the overall material color and any growth of decomposition products appears to be rather slow, peak integration changed only from 0.02 to 0.06 when referenced to the main peak at -19.1ppm.

Considering the time dependence to produce a single product based on the different milling speeds shown in the previous set of experiments, it seemed feasible that by reducing the milling times at higher rpm should complete the reaction in a shorter period of time. This concept was explored in Rxns #27, 29-41 (Table 4). The initial experiment (Rxn #27) at 250rpm, using the 15mm milling balls and a 1h cycle, gave a material of purple color and an ^{11}B NMR shift at -19.5ppm. Due to color the material was milled for another hour resulting in a noticeable color change to a light blue. The ^{11}B NMR main peak shifted to -19.3ppm and two peaks (-20.7 and -35.8ppm) associated with the decomposition of the sought-after product appeared.

Next the milling time was reduced to two only cycles of 45min, with a 30min rest time in between as a cooling period before the next cycle. Still, similar results across all milling ball sizes (Table 4, Rxn #29-31) were obtained with purple color appearance of the resulting materials. Milling time was further reduced while milling speed was increased up to 325rpm (Table 4, Rxn #32-40) resulting in a white solid showing a single peak in the ^{11}B NMR (Table 4, Rxn #32 and #36) for the 15mm milling ball, while all the reactions with either 10 or 20mm milling balls produced purple materials and at speeds above 250rpm showed decomposition products already forming after the initial run. At 325rpm even milling with the 15mm milling balls show signs of decomposition and/or purple color of the solids (Table 4, Rxn #40).

Due to the lengthy time periods to run and analyze the reactions, an additional new milling jar and milling balls were acquired to allow a higher reaction throughput. Since the new milling balls weighed slightly more than the previous set (76.20 g vs 74.00 g), the possibility of obtaining different results using identical reaction conditions was apparent. A milling was performed to determine the outcome of using a different ball weight to reactant mass ratio (Table 4, Rxn #41). It has to be noted that the milling time needed to increase using new balls and a new jar (an extra 20min of milling time was needed to complete the reaction), which strongly suggests that other forces, such as the difference in surface area and roughness of different milling equipment and balls, play a significant role in the speed of reaction.

One more aspect explored was varying the amount of reactants in the milling jar (Table 4, Rxn #42 and #43). For Rxn #42, the amount of materials was cut in half (5 mmol of both reagents). After milling at 250rpm the ^{11}B NMR showed that a substantial amount of decomposition products formed. For Rxn #43 the amount of materials was doubled (20mmol of both reagents) and according to ^{11}B NMR results it took overall longer to complete the reaction but no decomposition products were detected.

After the successful synthesis and optimization of the reactions to produce sodium and lithium amidoborane (NaNH$_2$BH$_3$ and LiNH$_2$BH$_3$, respectively) was completed, the research of potential coordination compounds was explored.   Through our previous work it was anticipated that displacement of the amino moiety of the compound when treated with higher boiling amines would occur. Due to a literature report that showed a coordination compound between LiNH$_2$BH$_3$ and hydrazine according to equation (2), this reaction was investigated first.

$$\text{LiNH}_2\text{BH}_3 + x\ \text{N}_2\text{H}_4 \longrightarrow \text{Li(N}_2\text{H}_4)x[\text{NH}_2\text{BH}_3]\ (x=1, 2) \qquad (2)$$

Our first experiment used the solid substrate of the sodium analog which was added to an excess of hydrazine. This mixture was allowed to stir for 48h at room temperature, after which, there was a noticeable second quartet forming at approximately -14.5ppm in the coupled [11]B spectrum (Figure 37(a)). If a simple coordination to the sodium cation would be taking place, there should not be a second peak forming in the ^{11}B NMR. Furthermore, this peak can be seen growing as time and temperature is applied

33

to the mixture (Figure 37(b-d)). After roughly 6d (Fig. 37(d)), near complete conversion to the hydrazine-borane complex is observed according to equation (3). This conversion was also observed, when reacting $LiHN_2BH_3$ with hydrazine in THF.

$$NaNH_2BH_3 + x\ N_2H_4 \longrightarrow NaHN\text{-}NH_2BH_3 \qquad (3)$$
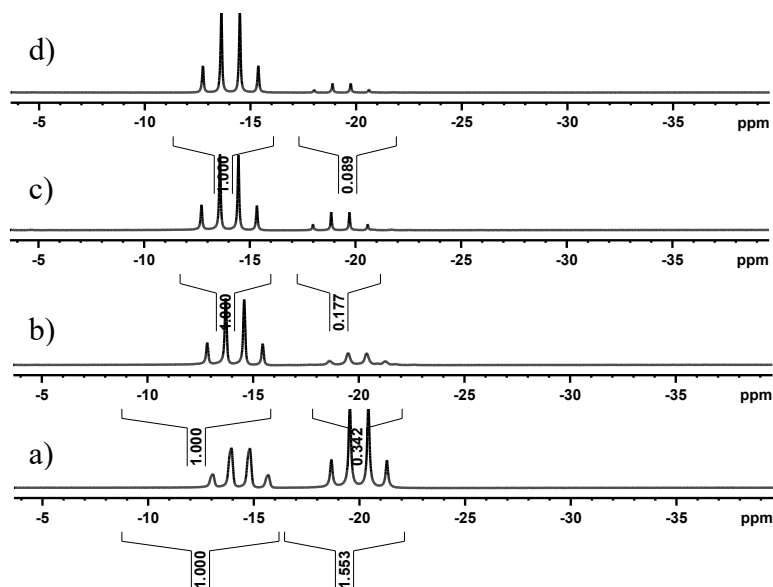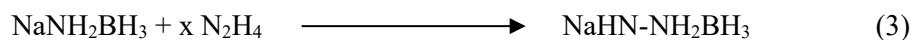
Figure 37. Reaction of hydrazine and amidoborane after: (a) 48h (b) +8h, 50°C (c) +72h, 50°C (d) +12h, 40°C

In general, this method may allow for the facile synthesis of different hydridoboranes.

Next, an exploration of the synthesis of the higher homologues of amidoboranes was undertaken via ball milling. The two next simplest anionic targets that had been reportedly produced in solution are $[BH_3NH_2BH_3]^-$ and $[BH_3NH_2BH_2NH_2BH_3]^-$. The methodology employed was similar to that used for the synthesis of the simple amidoboranes and followed the reactions (4) and (5).

$$MH + 2\ NH_3BH_3 \longrightarrow M[BH_3NH_2BH_3] + NH_3 + H_2\ (M=Na,\ Li) \qquad (4)$$
$$MH + 3\ NH_3BH_3 \longrightarrow M[BH_3NH_2BH_3NH_2BH_3] + NH_3 + H_2\ (M=Na,\ Li) \qquad (5)$$

For reaction (4), it was discovered that until milling speeds reach 325rpm, no reaction takes place. This is in contrast to the formation of amidoborane, which is produced at milling speeds as low as 200rpm. It is conceivable that due to the excess aminoborane in the reaction mixture that an initial formation of some amidoborane is undetected in the ^{11}B NMR spectrum. After reaching a milling speed of 325rpm, the reaction started to proceed. The initial milling of the material was performed for 45min and a slight shift in the ^{11}B spectrum as well as a visible change in the ^1H NMR was noted. Additional short milling cycles showed very little change in either the ^1H or ^{11}B NMR.

34

To elucidate whether the reaction was complete, extended milling cycles were carried out. After 4h of milling the reaction appeared to be similar to what was observed during the shorter runs, however, after 8h of milling, there is a very noticeable triplet that forms at ~-9ppm. This peak correlates with the formation of $[BH_3NH_2BH_2NH_2BH_3]^-$, the product of reaction (5). After 12h, this peak is becoming even
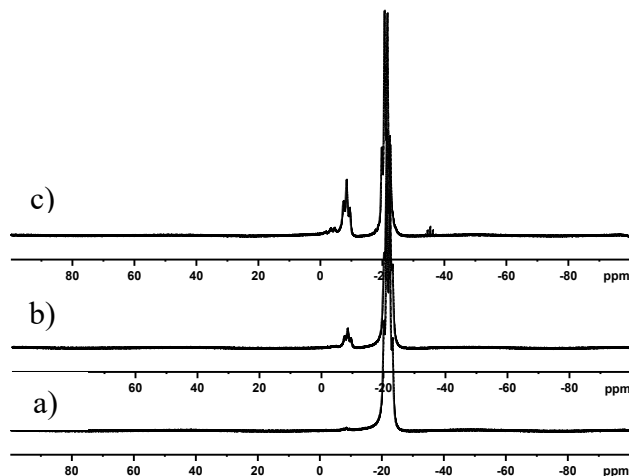
Figure 38. ^{11}B NMR of LiH + 2 NH_3BH_3 after: a) 4h b) 8h c) 12h hours

more noticeable (Figure 38). The formation of this product was unexpected considering the stoichiometry of the materials employed.

With the results from the previous reaction, it was anticipated that reaction (5) would take an extended period of time at 325rpm. Therefore, the initial speed pursuing the longer chain product according to equation (5) was set at 375, with the expectation that the reaction would still be slow. The decoupled ^{11}B NMR after an initial milling of 18h shows that the reaction was proceeding as expected, however, $[BH_4]^-$ is also being formed, Figure 39(b). Upon a further milling cycle of 18h, the ^{11}B NMR signals change, one of the two overlapping peaks at ~-21 ppm is clearly disappearing, Figure 39(c). Another peak begins to grow at ~-17 ppm, which could not be assigned to a specific product this time. After a total of 68h, the reaction predominately resulted in the formation of the unidentified compound.
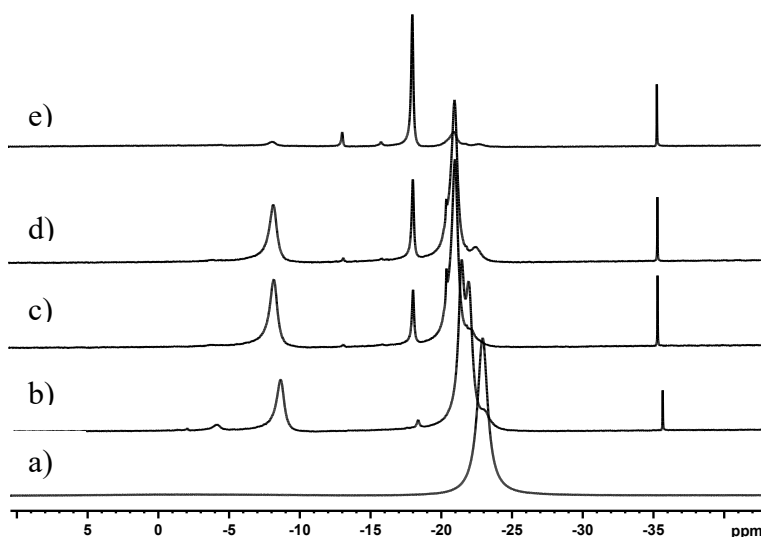
Figure 39. ^{11}B NMR of LiH + 3 NH_3BH_3 after: a) NH_3BH_3 b)18h c)36h d)54h e)68h

35

Summary

The process to mill sodium hydride and aminoborane to form sodium amidoborane has been studied in detail. The same methodology has been employed to optimize the reaction between lithium hydride and aminoborane. There are many variables in a milling system that need to be investigated in order to get a reproducible product (weight, size of milling balls, milling times, etc) and this can be a very time-consuming process employing air sensitive reagents. Many papers have been written on mechanochemical chemistry without providing any details on the conditions employed. Often, these papers make it sound like mechanochemical ball milling is a straightforward process changing the way we do chemistry today, being solvent free, environmentally friendly, simple to do, and with breakthrough results. Unfortunately, these papers only tend to scratch the surface of the problems involved during mechanochemical chemistry, relying on insufficient analytical results and reporting on new product formation without addressing issues of purification and scalability. Our results indicate that there is a huge potential for mechanochemical chemistry, but issues need to be addressed. Detailed parameters need to be established which is a very tedious, time-consuming process and requires the dedication of the chemist involved in the experiment. Unfortunately, published results cannot be taken for granted in this highly demanding area of research.

Our future work will revolve around repeatability and scalability of materials of interest and ones established move into new and exciting coordination chemistry of both sodium- and lithium-based hydrogen carrier, anionic species with various nitrogen and oxygen containing ligands (simple amines, ethers, heterocycles, etc).

Future synthetic targets based on an extended aminoborane framework will be investigated as well. The isolation and characterization of the products associated with the reaction to form $[BH_3NH_2BH_2NH_2BH_3]^-$ is expected to be completed soon. Also, during the initial screening of $[BH_3NH_2BH_3]^-$, the possibility of the desired material being produced may have been overlooked. This compound will once again be investigated and this time, the materials formed will be characterized after different milling times to determine whether the desired compound was obtained. Finally the synthesis of aminoborane cations will be investigated, with the known $[NH_3BH_2NH_3]^+$ cation as the initial target.

36

2.0   TASK II: IL Catalytic Reactivity & Ignition Chemistry

The goals of this research are to gain fundamental insight into 1) the catalysis and ignition mechanisms of mono- and bi-propellant ionic liquids (IL) and 2) the chemistry and physical properties of potential multi-mode propellant candidates. These investigations included both experimental (rapid-scan FTIR spectroscopy, thermogravimetric analysis mass spectrometry, tunable vacuum ultraviolet-photoionization (VUV-PI) mass spectrometry, high-resolution atmospheric pressure mass spectrometry and size-selected metal anion cluster photoelectron spectroscopy) and theoretical approaches (*ab initio*, direct molecular dynamics and machine learning qualitative structure property relationship (QSPR) methods). The identification of common reactive intermediates and energetic bottlenecks leading to ignition can aide in optimizing ignition properties for new propellant candidates. We also seek to understand anomalous behavior in current protic ionic liquid propellants that can cause efficiency losses and premature aging in the current ASCENT monopropellant formulation.

These complementary experimental and theoretical results can be combined to further develop detailed kinetics models which will allow for first-principle predictions of composition, temperature, and pressure effects to achieve reliable ignition in yet-to-be synthesized ILs and DESs fuels. Obtaining fundamental understanding at a molecular level of the ignition chemistry of IL and DES fuels is a key to the development of high-accuracy theoretical models for both catalytic and hypergolic ignition for supporting emerging Air Force priorities in in-space chemical propulsion.

2.1 Introduction: Task II Catalytic Reactivity & Ignition Chemistry Research

Energetic ionic liquids (EIL) and deep eutectic solvents (DES) are emerging technologies with the potential to replace hydrazine for propulsion and power. These next-generation propellants are being developed by the Air Force and considered by other agencies (e.g., NASA and MDA) for both monopropellant and bipropellant applications, where monopropellants, which contain both the fuel and oxidizer in one liquid, are decomposed and ignited over a catalyst bed and where bipropellants involve spontaneous ignition via mixing the fuel with a suitable oxidizer. The theoretical performance of EILs have been compared with hydrazines, which are the current, state-of-the-art fuels of choice in both monopropellant and bipropellant applications. For example, in the case of the EIL monopropellant formulation ASCENT (formerly known as AF-M315E), its density-specific impulse has been demonstrated to be 50% greater than that of hydrazine. These materials have the added benefit of greatly reduced vapor toxicity. For planned and emerging missions, hydrazines cannot provide sufficient thrust performance and has an unacceptable health and environmental footprint. Implementation of EIL/DES-based fuels would be in accordance with the green propellant initiative and would meet the demand for increased mission capabilities. NASA's first successful application of an ionic liquid monopropellant - the Green Propellant Infusion Mission - launched in June of 2019. While EILs and DESs show promise in both mono- and bipropellant systems, very little is understood about the fundamental chemistry that leads to ignition in both cases, especially the heterogeneous catalytic mechanisms of nitrogen-containing species. Additionally, the potentially higher adiabatic flame temperatures of these fuels (> 1800 $^\circ$C) and the corrosive nature of the combustion products (super-heated steam and CO_2) present a particular difficulty in catalyst material design that can withstand the extreme thermochemical environment during combustion. Of particular novelty is the recent push to use ionic liquids in a multi-mode propulsion (MMP) application, whereby a common propellant can be used as both a monopropellant in a chemical thruster *and* as an ion source in an electrospray ion thruster, allowing high thrust and high specific impulse missions, respectively. The in-space resiliency and superiority operability envelopes captured by MMP covers the range from chemical to electrochemical to electrostatic/electromagnetic propulsion. For MMP, not only tailoring the energy density of the liquid is important but also are its physical properties such as surface tension and electrical conductivity.

The scientific challenge addressed in this work is to understand the fundamental reaction mechanisms and reaction dynamics of the ignition and combustion of next-generation Air Force propellants. This challenge is important in addressing two general Air Force in-space priorities: resilience and superiority. Resilience simply means the ability of a space asset to survive and remain functional in a potentially contested space environment. Superiority refers, in general, to a space asset's ability to outperform other, potentially adversarial assets with particular emphasis on space situational awareness and space control. Both priorities are captured in the Rocket Propulsion for the 21st Century (RP21) Program goals and Space and Missile Systems Center (SMC) technology needs for in-space chemical propulsion. Increasing performance, extending thruster lifetimes and improving thruster reliability as well as reducing fuel toxicity are important objectives for RP21 and SMC stakeholders. Therefore, in supporting our RP21 and SMC customers, the goal of this research is to identify key reaction pathways and reaction intermediates involved in hypergolic and catalytic ignition of emerging energetic-green propellants in order to develop accurate chemical kinetics/multi-physics models for these complex processes to attain thruster performance predictive capabilities. The approach described here includes a combination of complementary experimental and theoretical methods to achieve the technical goals of this work. In order to ensure reliable ignition and sustained combustion, a high-fidelity chemical kinetics model is required; Heterogeneous catalysis mechanisms and inclusion of N species in the chemical kinetics model are lacking currently. Proton transfer processes are believed to be involved in HAN electrosprays and HAN evaporation issues and in HEHN long-term storage issues. Another issue of interest is developing capabilities for the prediction of ionic liquid physical properties for MMP, which currently are, expensive, time-consuming and have limited accuracy. One approach that has been successful uses qualitative structure property relationship (QSPR) and machine learning to more accurately predict such ionic liquid physical properties as surface tension and electrical conductivity with significantly lower computational cost. Surface tension and electrical conductivity predictions enable screening for developing ionic liquids for use in MMP.

Achieving reliable ignition and sustained combustion in these propellants and enabling their use in multi-mode propulsion systems are important challenges for the Air Force and critical to the progress towards meeting the Rocket Propulsion 21 Program goals and SMC technology needs.

2.1.1 Task II Results: Monopropellants, Bipropellants, and Multi-Mode Propellant Candidates

2.1.1.1 Monopropellants

#### Photoelectron spectroscopy and ab initio calculations of hydroxylamine reacted with size-selected iridium cluster anions

Elucidating the multifaceted processes of molecular activation and subsequent reactions gives a fundamental view into the development of iridium catalysts as they apply to fuels and propellants, e.g., for spacecraft thrusters. Hydroxylamine, a component of the well-known hydroxylammonium nitrate (HAN) ionic liquid, is a safer alternative and mimics the chemistry and performance standards of hydrazine. The activation of hydroxylamine by anionic iridium clusters, Ir$_n^-$ ($n = 1 - 5$), depicts a part of the mechanism, where two hydrogen atoms are removed, likely as H$_2$, and [Ir$_n$(NOH)]$^-$ clusters remain. The significant photoelectron spectral differences between these products and the bare clusters illustrate the substantial electronic changes imposed by the hydroxylamine fragment on the iridium clusters. In combination with density functional theory (DFT) calculations, a preliminary reaction mechanism is proposed, identifying the possible intermediate steps leading to the formation of [Ir(NOH)]$^-$.

Observed mass spectrometric products guide the DFT effort. Size selection of each Ir$_n$(NOH)$^-$ (n=1-5) cluster is then carried out and the electron is photodetached by 266 nm photons and the energy distributions of the electrons are measured (Figure 1). Photodetachment thresholds and higher energy features in the PES spectra give insight into the structure of the products. The combination of determining the atomic formulas for the products from the mass spectrometer, determining possible lowest-energy structures and their vertical electron detachment energy (VDE) thresholds from DFT calculations and

computing the barriers involved on the potential energy surfaces will yield significant insight in the reaction of HA + Ir_n^- (n=1-5) that is directly applicable to the heterogeneous catalysis process involved in HAN ignition on an iridium catalyst.

The mass spectrum resulting from the interaction of HA with the anionic iridium clusters indicated that no intact HA molecules were observed in conjunction with the Ir_n^- clusters. Instead, the HA lost two hydrogen atoms, forming $[Ir_n(NOH)]^-$ cluster anions, as shown in reaction 1.

$$HA + Ir_n^- \text{ (n=1-5)} \rightarrow Ir_nO^- \text{ (n=1-5)} + Ir_n(NOH)^- \text{ (n=1-5)} \tag{1}$$
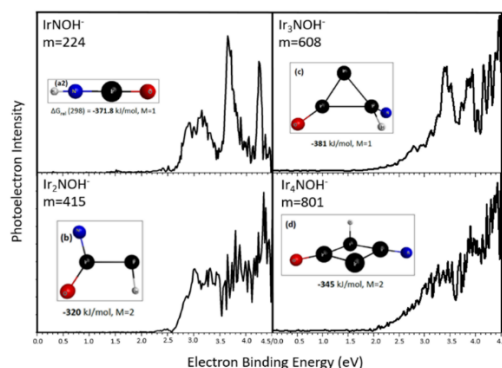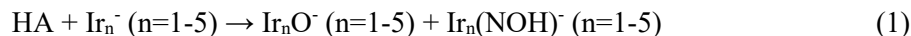
Figure 1. Photoelectron spectra of the $[Ir_n(NOH)]^-$ clusters (*n* =1-4) taken with the fourth harmonic of the Nd:YAG laser (266 nm, 4.66 eV). Insets are the lowest energy proposed structures for each species.

Calculations focused on identifying the most stable isomers of $[Ir_n\text{-}NOH]^-$, beginning with n=1. The isomers considered for n=1 included the unfragmented molecules HN=O (bonded to Ir by either the N or O atom) and N-OH, plus all possible combinations of N,H,O fragments, i.e., N+OH, NH+O, NO+H, and N+O+H, directly bonded to $[Ir]^-$, for a total of seven types of structural isomers. For each isomer, spin multiplicities of 1, 3, and 5 were considered
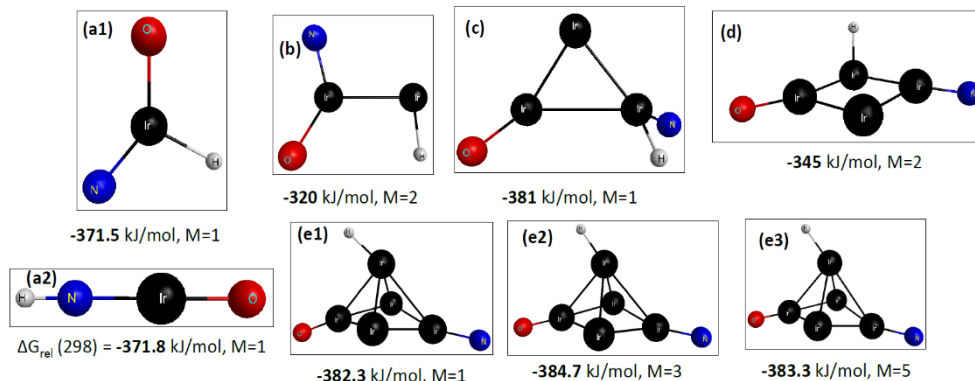
Figure 2. Lowest energy isomers of $[Ir_n\text{-}NOH]^-$; n=1-5. Free energies are at 298.15 K, relative to separated $[Ir_n]^- + NH_2OH - H_2$; i.e., ΔG for the reaction ($[Ir_n]^- + NH_2OH \rightarrow [Ir_n\text{-}NOH]^- + H_2$). M denotes the spin multiplicity.

The optimized structures of the two most stable isomers, $[Ir(O)(N)(H)]^-$ and $[Ir(O)(NH)]^-$, which have nearly equal relative free energies, are shown in Figure 2(a1) and (a2), respectively. The isomers in Figure 2(a1) and (a2) have a closed shell singlet ground state. The least stable isomers have unfragmented HN=O or N-OH moieties, with the partially fragmented isomers $[Ir(NO)(H)]^-$ and $[Ir(N)(OH)]^-$ having intermediate stabilities. Figure 3 summarizes the key steps in the proposed $[Ir]^- + NH_2OH$ mechanism.
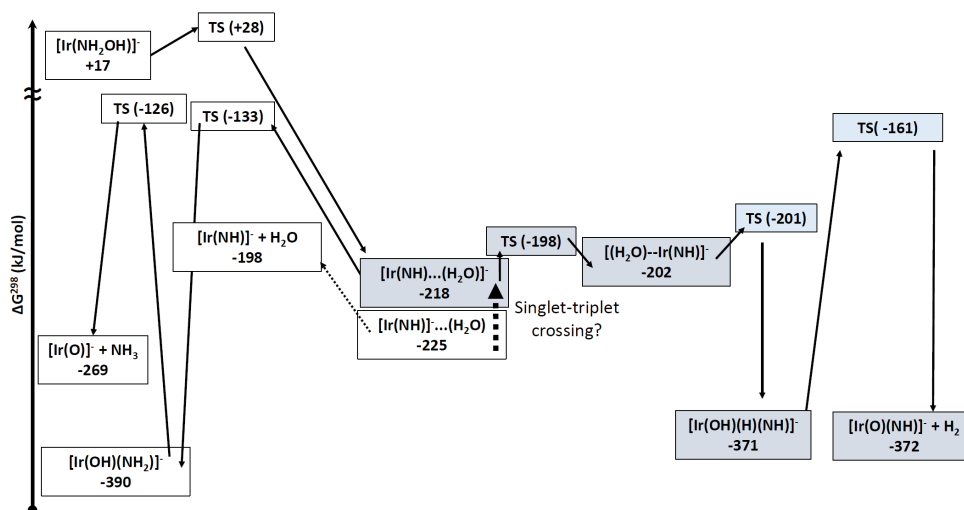
Figure 3. Potential energy diagram, not to scale, summarizing the key reaction steps leading to the formation of $[Ir(O)(NH)]^- + H_2$ and $[Ir(O)]^- + NH_3$. Free energies, in kJ/mol, are relative to $[Ir]^- + NH_2OH$. Unshaded boxes correspond to triplet states, whereas the blue-shaded boxes are singlet states.

In this work, photoelectron spectra of mass-selected bare Ir_n^- (n=1-5) anionic clusters and $[Ir_n(O)(NH)]^-$ (n=1-5) products were measured and the photoelectron VDEs were found to be in excellent agreement with DFT calculations. The reaction of Ir^- with hydroxylamine to form $[Ir(O)(NH)]^- + H_2$ is proposed to proceed through a triplet to singlet crossing and is exoergic by 372 kJ/mol. This pathway could help to explain the enhanced reactivity of hydroxylamine on iridium catalysts leading to large heat release and promoting ignition of HAN-based monopropellants. The systematic study of Ir_n^- with hydroxylamine offers a wealth of information as to the fundamental reaction mechanisms common to these heterogeneous catalytic reactions leading to combustion and ignition. This is critical in real world applications for continued design and development of the next generation fuels and catalysts, lowering the risks from exposure and explosive hazards and increasing the lifetime of the catalysts, thereby increasing the lifetime of the thrusters and spacecrafts as well.

The gas phase reaction of iridium and iridium carbide anions with 2-hydoxyethylhydrazine (HEH)
Understanding the chemistry of compounds that are similar to hydrazine has two advantages. First, it helps to identify less hazardous propellants to replace hydrazine as the most widely used monopropellant. And second, it helps to gain insight into the reaction mechanism that could be analogous to the decomposition of hydrazine into ammonia and nitrogen. Ionic liquids have already shown to be promising candidates to replace hydrazine. The molecule investigated in this study is 2-hydroxyethlyhydrazine ($HOCH_2CH_2NHNH_2$; HEH), which is a neutral precursor to the ionic liquid 2-hydroxyethylhydrazinium nitrate (HEHN) and differs from hydrazine by the substitution of a hydrogen with a hydroxyethyl group. Gas phase photoelectron spectroscopy and density functional theory were used to examine the reaction between a HEH molecule and an Ir^- anion as well as with IrC^-. Suggested by the experimental and theoretical data, Ir^- and IrC^- react with HEH and can attack the C-N, C-O, N-N, C-H and the C-C bond in HEH.
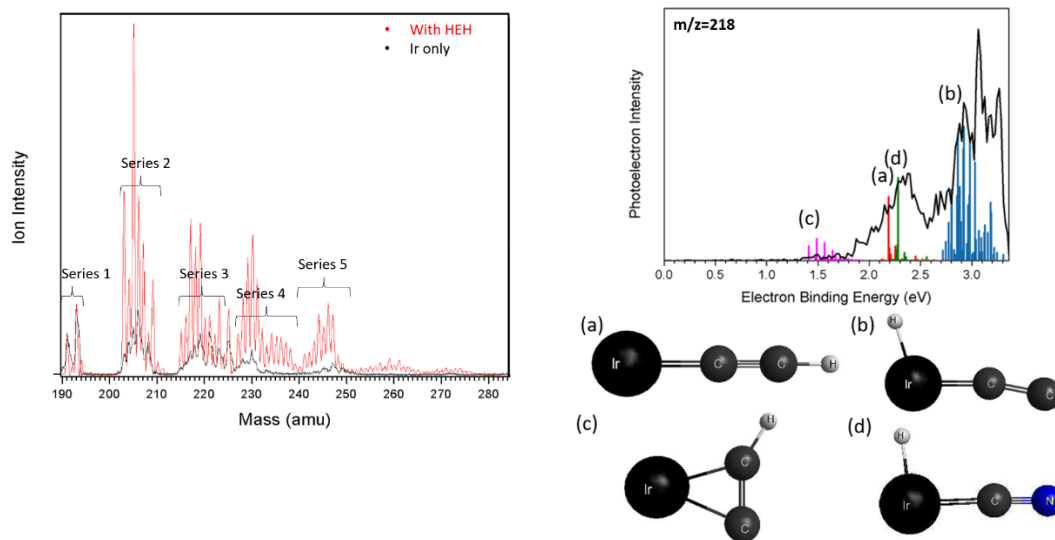
Figure 4. Left: Mass spectra of Ir_n^- (n=1-5, black trace) and $Ir_n^- + HEH$ (red trace). Right: Photoelectron spectrum of the m/z=218 species. The simulated PE spectra (colored lines) for three $^{193}IrC_2H^-$ isomers (with the relative Gibbs free energy a) $\Delta G_{rel}=0$ kJ/mol, b) $\Delta G_{rel}=90$ kJ/mol and c) $\Delta G_{rel}=91$ kJ/mol) and $^{191}IrNCH^-$ are included.

The gas phase study of the reaction of the iridium anion and HEH showed that the iridium anion can bond to different atoms in HEH. In this process, multiple bonds are broken with the extreme case where Ir^- can basically strip the carbon or nitrogen atoms of all other atoms. Cleavage of the N-N bond is supported by the theoretical data, the mass spectra and different photoelectron spectra. These reaction pathways also explain the observed products found in other studies such as hydrazine and ammonia, by breaking the N-C bond and the N-N bond in HEH, while providing hydrogen from breaking bonds at other points at the molecule. Ammonia for example could be formed, by breaking the N-N bond in HEH and releasing NH_2 which reacts with a hydrogen. This gives more insight in the actual mechanism of catalytic reactivity of HEH and might help to find out more about the hydrazine combustion, by indicating, that the N-N bond is broken in a reaction that is close to the combustion of hydrazine on an iridium-based catalyst.

Similar behavior as in the iridium-based interaction was observed with IrC^-. Using iridium carbide instead of pure iridium might be an effective way to lower the costs for monopropellant catalyst by using less of the rare iridium for the same amount of catalyst.

Thermal and Catalytic Decomposition of 2-Hydroxyethylhydrazine and 2-Hydroxyethylhydrazinium Nitrate Ionic Liquid

In order to develop chemical kinetics models for the combustion of ionic liquid-based monopropellants, identification of the elementary steps in the thermal and catalytic decomposition of components such as 2-hydroxyethylhydrazinium nitrate (HEHN) is needed but is currently not well understood. The first decomposition step in protic ionic liquids such as HEHN is typically the proton transfer from the cation to the anion, resulting in the formation of 2-hydroxyethylhydrazine (HEH) and HNO_3. In the first part of this investigation, the high temperature thermal decomposition of HEH is probed with flash pyrolysis (<1400 K) and vacuum ultraviolet (10.45 eV) photoionization time-of-flight mass spectrometry (VUV-PI-TOFMS). Next, the investigation into the thermal and catalytic decomposition of HEHN includes two mass spectrometric techniques: 1) tunable VUV-PI-TOFMS (7.4-15 eV) and 2) ambient ionization mass spectrometry utilizing both plasma and laser ionization techniques whereby HEHN is introduced onto a heated inert or iridium catalytic surface and the products are probed. The products can be identified by

their masses, their ionization energies, and their collision-induced fragmentation patterns. Formation of product species indicate that catalytic surface recombination is an important reaction process in the decomposition mechanism of HEHN. Selected products and their possible reaction mechanisms are discussed briefly below.

The flash pyrolysis of HEH results can be explained by two main pathways: 1) OH hydrogen to N2 migration yielding NH_3, H_2CO and $H_2C=NH$, and 2) N1H hydrogen to C1 migration from HEH1 or $HOCH_2CH_2N^+H_2N^-H$ to form $HOCH_2CH_3$ (Figure 4) that further decomposes to CH_3, H_3CCH or H_2CCH_2, C_2H_5 and H_2COH. The formation of $HOCH_2CH_3$ has not been previously proposed in the decomposition mechanism of HEH.
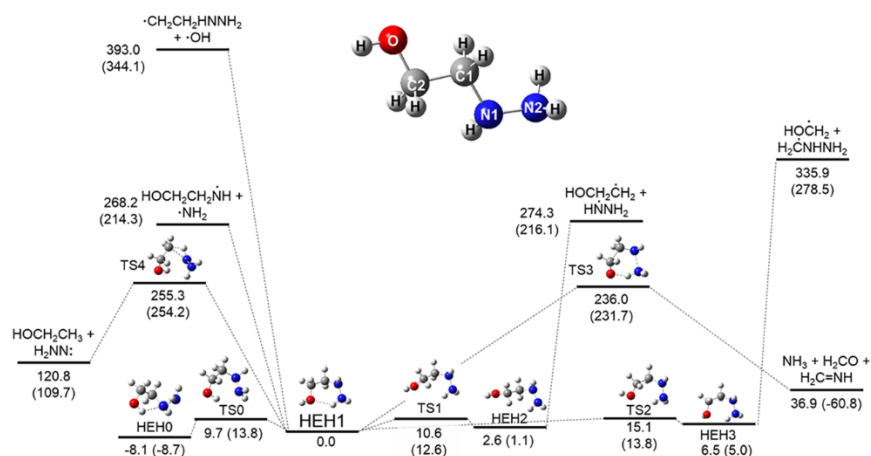

Figure 4. Atomic numbering and HEH thermal decomposition reaction profile. ΔH_{298} (ΔG_{298}) values calculated in kJ/mol at the M06/6-31+G(d,p) level of theory and are relative to HEH1.

The catalytic decomposition of HEHN on an iridium catalyst probed using tunable vacuum ultraviolet photoionization mass spectrometry indicates the catalytic enhancement of the formation of such stable products as NH_3, H_2O, N_2O (Figure 5b), HEH and HNO_3 and formation of radical species such as $\cdot CH_3$ and $\cdot C_3H_3$ (Figure 5a). Experiments using nanotip ambient ionization mass spectrometry (NAIMS) and CID showed the formation of ethanolamine and heavier product species upon the exposure of HEHN to a hot iridium catalyst (Figure 6 and Scheme 1).
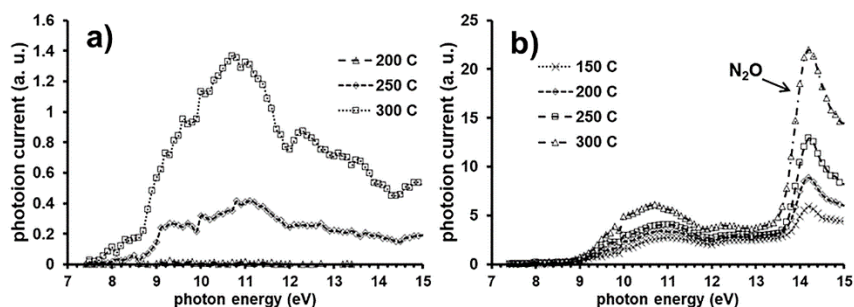
Figure 5. Photoionization efficiency curves of the catalytic decomposition of HEHN aerosols on an iridium catalyst as a function of temperature for a) *m/z* 39 and b) *m/z* 44 at 0.1 eV photon energy resolution. *M/z* 39 indicates the formation of $\cdot C_3H_3$, and the *m/z* 44 peak at 14.2 eV indicates the formation of N_2O.
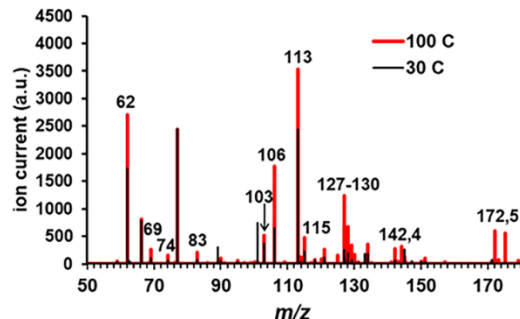
Figure 6. NAIMS spectra for HEHN on an iridium catalyst at 30 °C (black) and at 100 °C (red) from *m/z* 50-180.
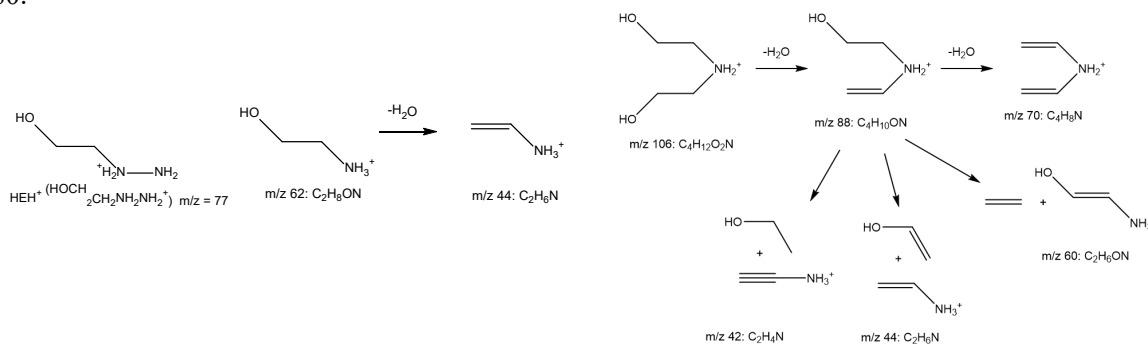

Scheme 1. Collision induced fragmentation (CID) patterns and possible chemical structures for masses 62.05968 (C₂H₈ON) and 106.08604 (C₄H₁₂O₂N) detected from nanotip ambient ionization mass spectrometric analysis of HEHN on an Ir catalyst at 100 °C. Note that the dihydroxyethylammonium cation (*m/z* 106) is observed as a product in the accelerated aging of TEAN.

This work describes experiments performed on the decomposition of HEHN and on 2-hydroxyethylhydrazine, the molecular precursor and primary thermal decomposition product of HEHN. Products observed experimentally and identified through DFT calculations and MD simulations are generally consistent with previous studies of HEH and HEHN. Herein, we have identified several new chemical species from thermal and catalytic decomposition processes, perhaps of most significance is the observation of ·CH₃ and propargyl radical (·C₃H₃) formation, and these species are believed to lead to recombination reactions resulting in products with higher masses than the original HEH reactant. Other reactions of significance are the heterogeneous dehydration and de-amination reactions and possible vinyl or hydroxyethyl addition reactions. Finally, the formation and subsequent decomposition of ethanol upon homogeneous, unimolecular thermal decomposition of HEH may proceed through a non-statistical, dynamic process. These products could be important in developing improved chemical kinetics models for catalytic ignition and combustion of HEHN-based monopropellants, and incorporation of these species into the kinetics models could result in improved fidelity for predictions of monopropellant thruster performance. Additional theoretical work is needed to understand such observations as the transformation of C₂ to C₃ to form the propargyl radical and the formation of N₂O in the catalytic reaction of HEH on an iridium catalyst.

HEHN thermal decomposition and kinetics via TGA-MS and TGA-FTIR

The objective of this work was to investigate the kinetics of 2-hydroxyethylhydrazinium nitrate (HEHN) thermal decomposition using thermogravimetric analysis (TGA) and differential scanning calorimetry (DSC) as well as to identify the evolved gas products with mass spectrometry (MS) and Fourier transform infrared (FTIR) spectroscopy (Figure 7). Both TGA and DSC have revealed that the decomposition of high-purity HEHN has two distinct stages. The effective kinetic parameters of both

43

stages were determined using the Ozawa-Wall-Flynn, Kissinger, and model-based methods. The model-based analysis has shown autocatalytic behavior of the involved reactions and produced apparent activation energies of 113.7 ± 1.7 kJ/mol at the first stage and 123.6 ± 2.5 kJ/mol at the second stage, close to the literature data (124.8 kJ/mol) on the autocatalytic reaction between HEHN and HNO_3. The evolved gas analysis (Figure 7) has shown that the first stage generates H_2O, N_2, NH_3, NO, N_2O, and NO_2, while the second stage also generates HNO_3 and CO_2. The observed existence of two stages in the thermal decomposition of HEHN could be explained by the formation of a condensed byproduct, which, in turn, decomposes via a highly activated reaction during the second (high-temperature) stage. These results can be used as inputs for an improved chemical kinetics model for ASCENT modeling and simulation.
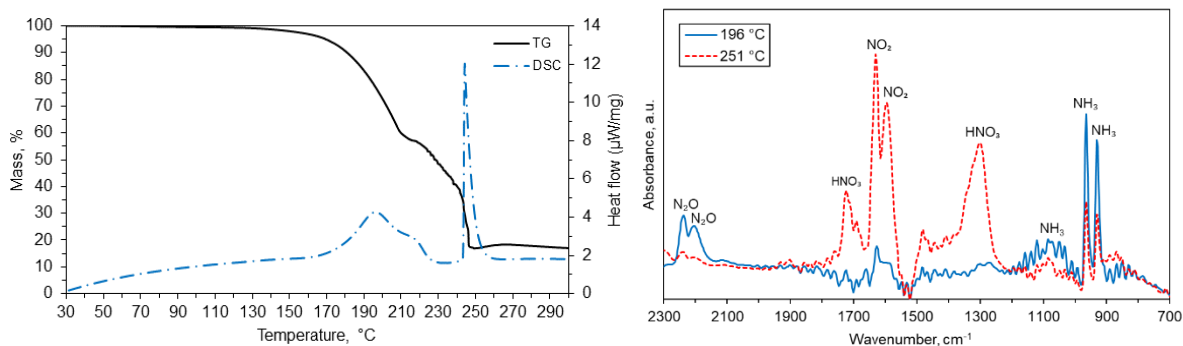

Figure 7. *Left:* TG and DSC curves of HEHN decomposition at 10 °C/min. *Right:* FTIR spectra of gases evolved at 196 °C and 251 °C during TGA of HEHN at a heating rate of 10 °C/min.

2.1.1.2 Bipropellants

Increased hypergolic reactivity of DCBH$^-$-based ionic liquids

In this study, *in situ* infrared spectroscopy techniques and thermogravimetric analysis (TGA) are employed to characterize the hypergolic reactivity of the ionic liquid, 1-butyl-3-methylimidazolium dicyanoborohydride ($BMIM^+DCBH^-$), in comparison to the well characterized 1-butyl-3-methylimidazolium dicyanamide ($BMIM^+DCA^-$) ionic liquid. TGA measurements were used to determine the enthalpy of vaporization (ΔH_{vap}), that was calculated to be 112.7 ± 12.3 kJ/mol at 298 K and is relatively low compared to other ionic liquids. A rapid scan Fourier transform infrared (FTIR) spectrometer was used to take numerous spectra throughout the hypergolic reactions of $BMIM^+DCBH^-$ and $BMIM^+DCA^-$ with white fuming nitric acid (WFNA, Figure 8) and during thermal decomposition of these energetic ionic liquids (EILs) to track the appearance and disappearance of potential key components. Computational chemistry efforts were paired with the experimental results to propose key reaction pathways leading to the ignition of these combinations. Results show $BMIM^+DCBH^-$ has certain key intermediates leading to ignition with WFNA that differ from those seen for $BMIM^+DCA^-$. Nitrous oxide was generated during both reactions, indicating that it may play a crucial role in the hypergolic ignition process. HCN is proposed to be generated during both thermal decomposition and hypergolic ignition of $BMIM^+DCBH^-$ (Figure 9).
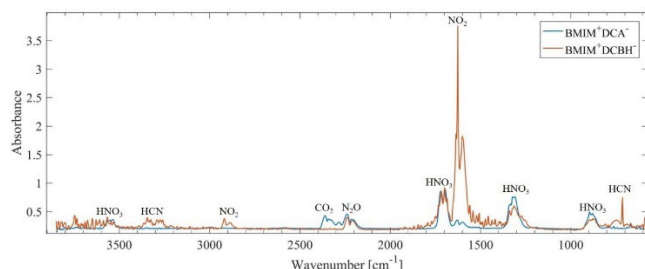
Figure 8. FTIR spectra obtained for BMIM⁺DCBH⁻ (red) and BMIM⁺DCA⁻ (blue) in reaction with white fuming nitric acid (WFNA) shortly after mixing.
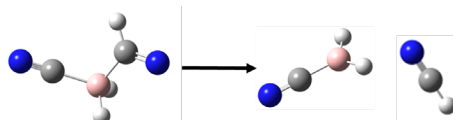
Figure 9. Formation of HCN through the protonation of the DCBH⁻ at the carbon, where 92 kJ/mol of free energy is released.

Molecular dynamics investigations of hypergolic reactivity of DCA⁻ and DBCH⁻-based ionic liquids with HNO₃

In order to fully understand the differences in the hypergolic ignition mechanisms between DCA⁻ and DBCH⁻ described above, direct molecular dynamics simulations of HNO₃ with DCA⁻ (i.e., N(CN)₂⁻) and DCBH⁻ (i.e., BH₂(CN)₂⁻) were performed at the B3LYP/6-31+G(d) level of theory in an attempt to elucidate the primary and secondary reactions in the two reaction systems. Guided by trajectory results, reaction coordinates and potential energy diagrams were mapped out for the oxidation of DCA⁻ and DCBH⁻ by one and two HNO₃ molecules, respectively, in the gas phase and in the condensed-phase ionic liquids using the B3LYP/6-311++G(d,p) method. The oxidation of DCA⁻ by HNO₃ is initiated by proton transfer. The most important pathway leads to the formation of $O_2N-NHC(O)NCN^-$, and the latter reacts with a second HNO₃ to produce $O_2N-NHC(O)NC(O)NH-NO_2^-$ (DNB⁻), consistent with previous work.
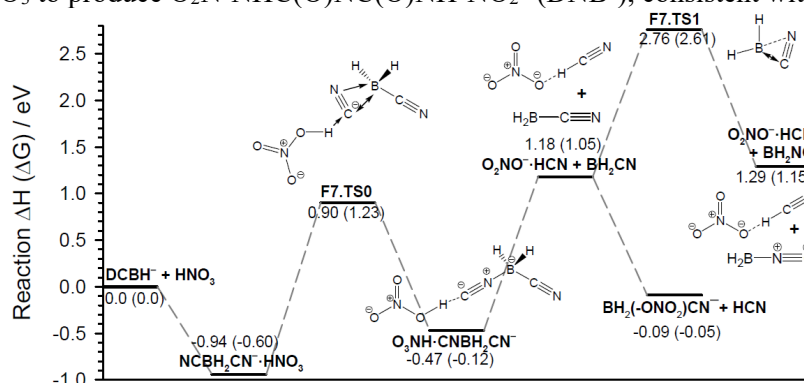
Figure 10. Reaction coordinates for the isomerization of DCBH⁻ with one HNO₃.

The oxidation of DCBH⁻ by HNO₃ may follow a similar mechanism as DCA⁻, producing two analogue products: $O_2N-NHC(O)BH_2CN^-$ (Figure 10) and $O_2NNHC(O)BH_2C(O)NH-NO_2^-$. Moreover, two new, unique reaction pathways were discovered for DCBH⁻ due to its boron-hydride group: 1) Isomerization of DCBH⁻ to $CNBH_2CN^-$ and $CNBH_2NC^-$; and 2) H₂ elimination in which the proton in HNO₃ approaches and combines with a hydride-H in DCBH⁻. Rice-Ramsperger-Kassel-Marcus (RRKM) theory was utilized to calculate reaction rate constants and branching ratios among various product channels. The RRKM results indicate that the formation of DNB⁻ is exclusively important in the oxidation of DCA⁻, whereas

the same type of reaction is a minor channel in the oxidation of DCBH⁻. In the latter case, H₂ elimination becomes dominating. The RRKM modeling also indicates that the oxidation rate constant of DCBH⁻ is higher than that of DCA⁻ by an order of magnitude. This rationalizes the enhanced preignition performance (shorter ignition delay time) of DCBH⁻ over DCA⁻ with HNO₃.

2.1.1.3 Multi-Mode Propellants

HEHN cluster structure investigation via cold ion IR spectroscopy of ionic liquid clusters
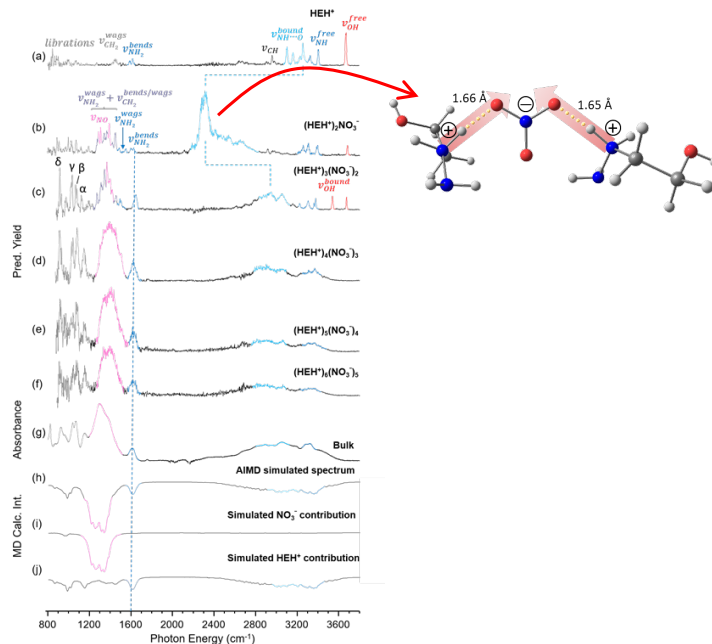
Figure 11. Vibrational predissociation spectra of D₂-tagged (a) HEH⁺ and (b-f) $(HEH^+)_n(NO_3^-)_{n-1}$ with n = 2-6. FTIR spectrum of the bulk IL is shown in trace (g). AIMD simulated spectrum of the neutral (15,15) cluster (h) for 20 ps with individual contribution of the NO_3^- anions and HEH⁺ cations separated and displayed inverted in (i) and (j), respectively.

One major drawback from using HEHN as one component of the ASCENT monopropellant fuel is that pure HEHN tends to turn brown over time, and this could be attributed to a lower ionicity of HEHN due to proton transfer from the cation to the anion and subsequent irreversible reactions of the neutral species to unwanted products. In order to better understand why HEHN has a limited shelf-life, it is useful to look at the local structure of the ions in the liquid. With this in mind, we determined the intramolecular distortions at play in the 2-hydroxyethyhydrazinium nitrate (HEHN) ionic liquid (IL) propellant, which presents the interesting case that the HEH⁺ cation has multiple sites (i.e., hydroxy, primary amine and secondary ammonium groups) available for H-bonding with the nitrate anion. These interactions are quantified by analyzing the vibrational band patterns displayed by cold cationic clusters, $(HEH^+)_n(NO_3^-)_{n-1}$, n = 2-6, which are obtained using IR photodissociation of the cryogenically cooled, mass-selected ions. The strong interaction involving partial proton transfer of the acidic N-H proton in HEH⁺ cation to the nitrate anion is strongly enhanced in the ternary n = 2 cluster (Figure 11b) but is suppressed with increasing cluster size (Figure 11c-f). The cluster spectra recover the bands displayed by the bulk liquid by n = 4, thus establishing the minimum domain required to capture the macroscopic (bulk) behavior. The partial proton transfer observed in the $(HEH^+)_2(NO_3^-)$ cluster could indicate reduced

46

ionicity and higher equilibrium concentrations of the neutral HEH and HNO_3 species that can subsequently react further to unwanted side products.

Structures, Proton Transfer and Dissociation of the Hydroxylammonium Nitrate Species Revealed by Electrospray Ionization Mass Spectrometry and Dynamics Simulations

Hydroxylammonium nitrate (HAN) is a promising, green alternative to hydrazine in spacecraft applications. It is also a candidate for dual-mode propulsion systems, which combine both chemical and electrospray thrust capabilities of a monopropellant blend of HAN and ionic liquid. However, the electrospray properties of neat HAN are not well understood. Capitalizing on electrospray ionization (ESI) and collision-induced dissociation (CID) measurements using a guided-ion beam tandem mass spectrometer, and augmented by molecular dynamics simulations, this work characterizes structures and reaction dynamics of the HAN species in the gas phase that mimics those found in low earth orbit and outer space. The HAN monomer adopts a stable covalent structure $HONH_2 \cdot HNO_3$ in the gas phase. Proton transfer between the $HONH_2$ and HNO_3 moieties can be induced by adding a NO_3^- anion, leading to the formation of $^-O_3N \cdot HONH_3^+ \cdot NO_3^-$ in negative electrosprays. In contrast, dissociative reactions occur when a proton approaches $HONH_2 \cdot HNO_3$ in the gas phase, leading to H_2O, NO_2 and $HONH_2$ fragments and their cations. As a result, no HAN species was detected in positive electrosprays. Unlike the covalent HAN monomer, the $(HAN)_2$ dimer undergoes double proton transfer spontaneously in the gas phase and forms an ionic *cyclic*-$[^-O_3N \cdot HONH_3^+ \cdot NO_3^- \cdot HONH_3^+]$ structure.

The negative ESI mass spectrum of HAN was dominated by NO_3^- and $HNO_3 \cdot NO_3^-$, both of which were detected in the anion mass spectra of the HAN/EMIM$^+$EtSO$_4^-$ mixture. A new species that was captured only in the negative ESI of pure HAN is the anion of *m/z* 158 as depicted in Figure 12a. To verify the structure of this new species, ions of *m/z* 158 were mass selected in the tandem mass spectrometer and subjected to collision-induced dissociation (CID) with the Xe gas under the single ion-molecule collision conditions. Tandem mass spectrometry was then utilized to measure dissociation product ions and dissociation threshold energetics, aimed at distinguishing and determining ion structures, stability and reaction pathways.
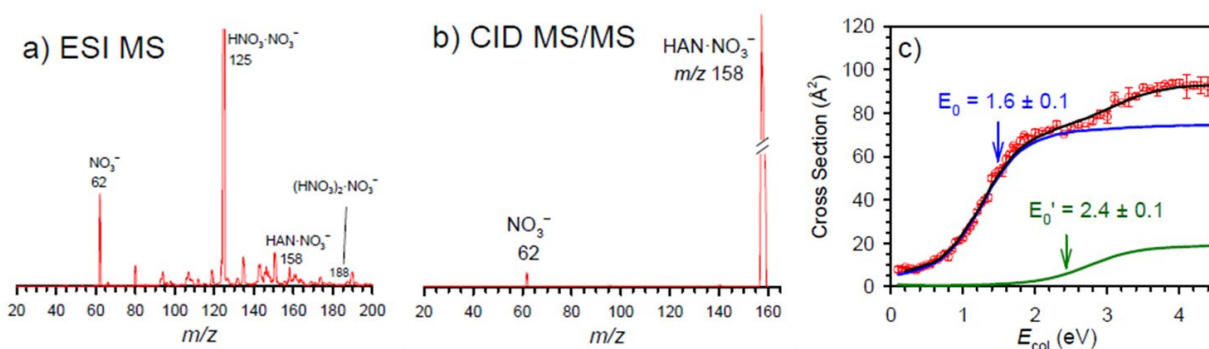
Figure 12. (a) Negative ESI mass spectrum of HAN in 3:1 acetonitrile/water; (b) Product ion mass spectrum for the CID of HAN·NO_3^- with Xe measured at $E_{col} = 3.0$ eV; and (c) cross sections of NO_3^- product ions as a function of E_{col} with Xe. Circles are experimental data (with error bars) and solid lines are theoretical fits where blue is channel 1, green is channel 2 and black is the sum of channel 1 + channel 2.

The CID of *m/z* 158 ions produced only NO_3^- fragment ions as demonstrated in Figure 12b. Based on the CID results, the new species was assigned as a HAN·NO_3^- cluster. Product ion cross sections were measured over a center-of-mass collision energy (E_{col}) range of $0.05 - 4.5$ eV. The result is presented in Figure 12c, wherein the error bars were determined based on four sets of measurements.

The CID cross section of HAN·NO$_3^-$ appears to consist of two components, with one dominating at the low E_{col} range and the other starting to emerge at high E_{col}. No satisfactory fit could be obtained with a single $\sigma(E_{col})$ function. We have therefore fit the cross section using two sets of $\sigma(E_{col})$ functions. E_0 and n of each set were adjusted independently to obtain the best fit to the total cross section. As shown by the blue- and green-color LOC fits and respective E_0 values indicated in Figure 12c, the first component has $E_0 = 1.6$ eV and $n = 2.4$, and the second component has $E_0 = 2.4$ eV and $n = 2.5$.

Quasi-classical direct dynamics trajectory results indicate that there are two collisionally activated structures coexisting at high E_{col}, that is $[^-O_3N\cdot HONH_3^+\cdot NO_3^-]^*$ (major) $\rightleftharpoons [O_3NH\cdot HONH_2\cdot NO_3^-]^*$ (minor). Accordingly, two CID product channels can be proposed as follows, for which reaction enthalpies (ΔH) were calculated at the ωB97XD/6-31+G(d,p) level of theory:

$$HAN\cdot NO_3^- \xrightarrow{Xe} [^-O_3N\cdot HONH_3^+\cdot NO_3^-]^* \rightarrow HONH_2\cdot HNO_3 + NO_3^- \quad \Delta H = 1.55 \text{ eV} \quad (3)$$

$$HAN\cdot NO_3^- \xrightarrow{Xe} [O_3NH\cdot HONH_2\cdot NO_3^-]^* \rightarrow HONH_2 + HNO_3 + NO_3^- \quad \Delta H = 2.24 \text{ eV} \quad (4)$$
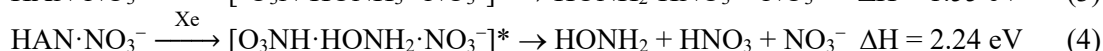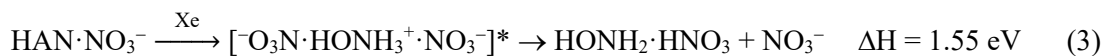
The product enthalpies of reactions (3) and (4) are in excellent agreement with the E_0 values we have determined in the CID experiment.

It is reasonable to assume that the populations of $[^-O_3N\cdot HONH_3^+\cdot NO_3^-]^*$ and $[O_3NH\cdot HONH_2\cdot NO_3^-]^*$ formed in the trajectories (total 100) correlate to some extent with the product branching ratio between reactions (3) and (4). Indeed, the trajectory-predicted ratio of $[^-O_3N\cdot HONH_3^+\cdot NO_3^-]^*:[O_3NH\cdot HONH_2\cdot NO_3^-]^*$ is 4:1, and this value has exactly matched the ratio of the LOC-fitted maximum cross sections for the two dissociation channels (see Figure 12c).

When the dimer of HAN is calculated, the lowest energy structure is ionic, and this is explained by the facile double proton transfer from $[HONH_2\cdot NO_3^-]_2$ to form $[HONH_3^+\cdot NO_3^-]_2$. This indicates that in the addition of NO_3^- to $[^-O_3N\cdot HONH_3^+\cdot NO_3^-]$, $[HAN]_2$ remains ionic in contrast to the HAN monomer which is most stable in its neutral from.

This work is the first ESI mass spectroscopic study of pure HAN, aimed at exploring what constituents are to be expected in electrosprays and what likely happens in the space-environment of electrospray thrusters. A HAN monomer maintains a stable covalent $HONH_2\cdot HNO_3$ structure in the gas phase. Proton transfer in $HONH_2\cdot HNO_3$ may be induced by an additional NO_3^-. Consequently, $^-O_3N\cdot HONH_3^+\cdot NO_3^-$ was detected in the anion ESI mass spectrum and its structure and dissociation dynamics were characterized using a combination of tandem CID mass spectrometry and molecular dynamics simulations. On the other hand, spontaneous double proton transfer was found in the dynamics simulations of the HAN dimer in the gas phase, leading to a *cyclic*-$[HONH_3^+\cdot NO_3^-\cdot HONH_3^+\cdot NO_3^-]$ structure. This work has also simulated the dissociative reaction of $HONH_2\cdot HNO_3$ with H^+ in the gas phase, from which we have rationalized the lack of intact HAN species in the cation ESI mass spectra. The combined experimental and theoretical study has showcased different reactivities of the HAN monomer and dimer. The results are of importance for modeling spacecraft thruster performance, such as in the understanding of the output of electrospray thrusters and of the fate of plume species after ejection into space.

Multi-Mode Propellants: Quantitative Structure Property Relationships for Predicting Ionic Liquid Physical Properties

Quantitative structure property relationship (QSPR) methods provide a low computational cost alternative to expensive molecular dynamics or quantum chemistry approaches to predicting physical properties (density, viscosity, melting point, etc.) of pure substances. QSPR has been previously applied to successfully predict viscosity and hypergolic ignition delay times for ionic liquids of interest to the Air Force. An AFRL SBIR-funded software package named ProDET uses machine learning and data mining to correlate experimental data with appropriate descriptors (generated by simple Gaussian quantum

48

chemical calculations). This technique has been recently employed to predict physical properties of ionic liquid propellant candidates for use in electrospray thruster applications. Specific impulse, I_{sp}, the performance metric of interest in electrospray propulsion, is proportional to the 4th root of both the surface tension and the electrical conductivity, and therefore ionic liquids with both high surface tension and electrical conductivity are desirable. These two physical properties are largely unknown for proposed ionic liquids of interest to the Air Force, so the capability to accurately - and at low cost - predict surface tension and electrical conductivity is a very useful screening tool for new ionic liquid development.
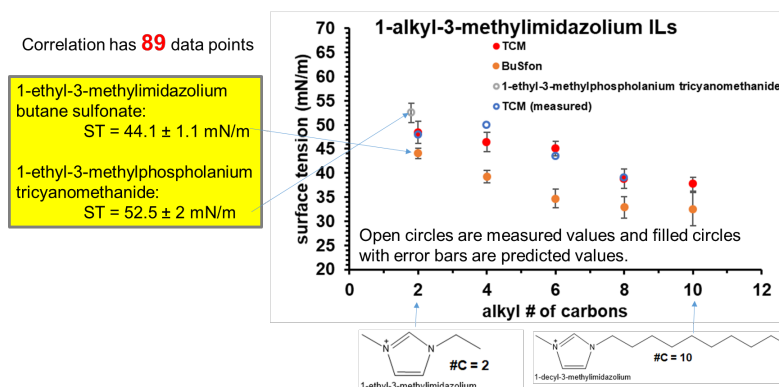
Figure 13. Quantitative structure property relationship (QSPR) predictions of surface tensions of ionic liquids for 1-n-alkyl-3-methylimidazolium cations (alkyl = C2, C4, C6, C8 and C10) paired with tricyanomethanide and butanesulfonate anions. The 1-ethyl-1-methylphospholanium cation is similar in size to the 1-ethyl-3-methylimidazolium cation and is shown here for comparison.

   In this work, 89 surface tension measurements from the literature were included in the correlations. A select subset of surface tension predictions are shown in Figure 13, where the surface tension values are predicted for 1-n-alkyl-3-methylimidazolium cations (n=C2, C4, C6, C8 and C10) paired with tricyanomethanide and butanesulfonate anions. The predictions show a trend that indicates the surface tension is reduced with increasing alkyl chain length and that the tricyanomethanide anions typically have a higher surface tension than butanesulfonate for a given cation. In Figure 13, there are four experimental data points in the blue circles, and these points match quite well with the predicted values, compared to the 95% confidence intervals of the error bars. The predicted surface tension values have assigned relative uncertainties of between 2.5% and 10.5%, and these errors can be further reduced by adding more data points to the correlation set. The two predicted points that are highlighted in Figure 13 are for 1-ethyl-3-methylimidazolium butanesulfonate and for 1-ethyl-3-methylphospholanium tricyanomethanide, and these are ionic liquids of interest to the Air Force and will be discussed in more detail below.
   Relative to surface tension data, here are fewer experimental measurements of electrical conductivity of ionic liquids in the literature, so the data set for electrical conductivity correlations contained 59 points. Figure 14 presents a similar analysis as Figure 13 but for electrical conductivity rather than for surface tension. Electrical conductivity trends are similar to surface tension in that the electrical conductivity decreases with increasing alkyl chain length in the methylimidazolium cation and the tricyanomethanide anion exhibits higher electrical conductivity in general versus butanesulfonate. For 1-ethyl-3-methylimidazolium butanesulfonate and for 1-ethyl-3-methylphospholanium tricyanomethanide, there exist measured values that are seen highlighted in Figure 14. While the error bars are somewhat large in Figure 14, they encompass the measured values well, indicating reasonable accuracy for these predictions with only 57 data points in the correlation. When compared to previously predicted values for these two ionic liquids (seen in red triangles in Figure 14), this QSPR method shows improved accuracy and has the benefit of greatly reduced computational expense over the previous predictive method (molecular dynamics).
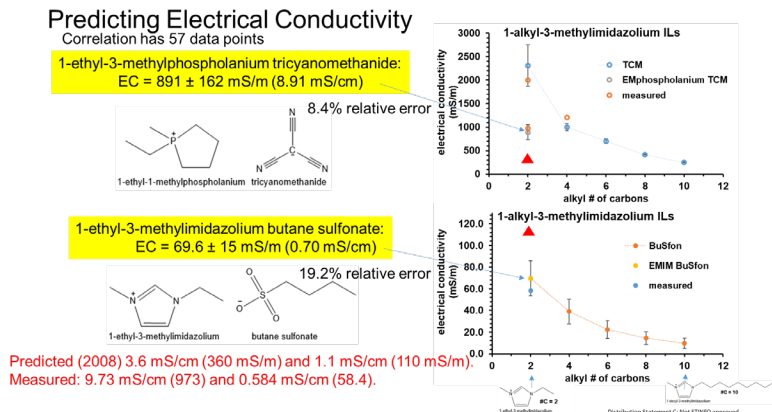
Figure 14. Quantitative structure property relationship (QSPR) predictions of electrical conductivities of ionic liquids for 1-n-alkyl-3-methylimidazolium cations (alkyl = C2, C4, C6, C8 and C10) paired with tricyanomethanide and butanesulfonate anions.

Sensitivity analysis of the descriptors used in the electrical conductivity correlations indicate that the single most sensitive descriptor is the fraction of hydrogens in the anion, where the electrical conductivity is inversely related to the fraction of hydrogens in the anion. This can help to explain why the tricyanomethanide $(C(CN)_3)^-$ and dicyanamide $(N(CN)_2)^-$ ionic liquids–having zero fraction of hydrogens–have such high electrical conductivities in general. These predictions indicate that the 1-ethyl-3-methylimidazolium tricyanomethanide ionic liquid, having both the highest surface tension and the highest electrical conductivity of the ionic liquids we studied, would be a good candidate propellant for electrospray propulsion.

Future work includes predicting the surface tension and electrical conductivity values for cyanoborohydride anion based ionic liquids $(BH_n(CN)_{(4-n)})^-$ (n=0-4), which have previously demonstrated rapid hypergolic ignition delay times with nitric acid. Based on the criterion of lower fraction of hydrogens in the anion mentioned above, it is predicted that the tetracyanoborate anion ionic liquids would have the highest electrical conductivities of all of the cyanoborohydride-based ionic liquids. This predictive approach may also be implemented to predict physical properties of deep eutectic solvent propellant candidates, and it can be adapted to incorporate novel descriptors such as those from the effective fragment potential (EFP) method.

3.0 Publications

1) Ciborowski, S. M.; Buszek, R.; Liu, G.; Blankenhorn, M.; Zhu, Z.; Marshall, M. A.; Harris, R. M.; Chiba, T.; Collins, E. L.; Marquez, S.; Boatz, J.A.; Chambreau, S.D.; Vaghjiani, G.L.; Bowen, K.H. Study of the Reaction of Hydroxylamine with Iridium Atomic and Cluster Anions (n = 1–5). *The Journal of Physical Chemistry A* **2021**, *125* (27), 5922-5932, DOI: 10.1021/acs.jpca.1c03935.
2) Blankenhorn, M.; Chiba, T.; Boatz, J. A.; Chambreau, S. D.; Ganteför, G.; Bowen, K. H., The gas phase reaction of iridium and iridium carbide anions with 2-hydoxyethylhydrazine (HEH). *International Journal of Mass Spectrometry* **2022**, *478*, 116875.
3) Chambreau, S. D.; Popolan-Vaida, D. M.; Kostko, O.; Lee, J. K.; Zhou, Z.; Brown, T. A.; Jones, P.; Shao, K.; Zhang, J.; Vaghjiani, G. L.; Zare, R. N.; Leone, S. R., Thermal and Catalytic Decomposition of 2-Hydroxyethylhydrazine and 2-Hydroxyethylhydrazinium Nitrate Ionic Liquid. *The Journal of Physical Chemistry A* **2022**, *126* (3), 373-394.

4) Esparza, A. A.; Chambreau, S. D.; Vaghjiani, G. L.; Shafirovich, E., Two-stage decomposition of 2-hydroxyethylhydrazinium nitrate (HEHN). *Combustion and Flame* **2020**, *220*, 1-6.

5) Burnette, M.; Chambreau, S. D.; Vaghjiani, G. L., Iridium Catalyst Detection by Laser Induced Breakdown Spectroscopy. *Spectrochimica Acta Part B: Atomic Spectroscopy* **2022**, 187, 106327.

6) Thomas, A. E.; Chambreau, S. D.; Redeker, N. D.; Esparza, A. A.; Shafirovich, E.; Ribbeck, T.; Sprenger, J. A. P.; Finze, M.; Vaghjiani, G. L., Thermal Decomposition and Hypergolic Reaction of a Dicyanoborohydride Ionic Liquid. *The Journal of Physical Chemistry A* **2020**, *124* (5), 864-874.

7) Zhou, W.; Liu, J.; Chambreau, S. D.; Vaghjiani, G. L., Molecular Dynamics Simulations, Reaction Pathway and Mechanism Dissection, and Kinetics Modeling of the Nitric Acid Oxidation of Dicyanamide and Dicyanoborohydride Anions. *The Journal of Physical Chemistry B* **2020**, *124* (49), 11175-11188, DOI: 10.1021/acs.jpcb.0c07823.

8) Thomas, A.; Chambreau, S. D.; Vaghjiani, G. L., Ignition Delay Reduction with Sodium Addition to Imidazolium-Based Dicyanamide Ionic Liquid. *The Journal of Physical Chemistry A* **2019**, *123* (1), 10-14.

9) Liu, J.; Zhou, W.; Chambreau, S. D.; Vaghjiani, G. L., Molecular Dynamics Simulations and Product Vibrational Spectral Analysis for the Reactions of NO_2 with 1-Ethyl-3-methylimidazolium Dicyanamide ($EMIM^+DCA^-$), 1-Butyl-3-methylimidazolium Dicyanamide ($BMIM^+DCA^-$), and 1-Allyl-3-methylimidazolium Dicyanamide ($AMIM^+DCA^-$). *The Journal of Physical Chemistry B* **2020**.

10) Liu, J.; Zhou, W.; Chambreau, S. D.; Vaghjiani, G. L., Computational Study of the Reaction of 1-Methyl-4-amino-1,2,4-triazolium Dicyanamide with NO2: From Reaction Dynamics to Potential Surfaces, Kinetics and Spectroscopy. *The Journal of Physical Chemistry B* **2019**, *123* (13), 2956-2970.

11) Zeng, H. J.; Khuu, T.; Chambreau, S. D.; Boatz, J. A.; Vaghjiani, G. L.; Johnson, M. A., Ionic Liquid Clusters Generated from Electrospray Thrusters: Cold Ion Spectroscopic Signatures of Size-Dependent Acid–Base Interactions. *The Journal of Physical Chemistry A* **2020**, *124* (50), 10507-10516, DOI: 10.1021/acs.jpca.0c07595.

12) Zhou, W.; Liu, J.; Chambreau, S. D.; Vaghjiani, G. L., Structures, proton transfer and dissociation of hydroxylammonium nitrate (HAN) revealed by electrospray ionization tandem mass spectrometry and molecular dynamics simulations. *Physical Chemistry Chemical Physics* **2022**, *24* (22), 14033-14043.

13) Vaghjiani, G. L.; Sun, H.; Chambreau, S. D., Experimental and Theoretical Investigations of the Radical–Radical Reaction: $N_2H_3 + NO_2$. *The Journal of Physical Chemistry A* **2020**, *124* (50), 10434-10446, DOI: 10.1021/acs.jpca.0c07985.

14) Ferguson, R. E., Esparza, A. A., Chambreau, S. D., Vaghjiani, G. L., Shafirovich, E., Studies on the Combustion of HAN/Methanol/Water Propellants and Decomposition of HAN and HEHN. *International Journal of Energetic Materials and Chemical Propulsion* **2021**, *20* (2), 21-31.

4.0 Presentations

1. Chambreau, S. D., "Heterogeneous Catalysis of Ionic Liquids," 2022 Department of Defense 6.1 Basic Research Conference (BRICC), September 6-9, 2022.

2. Stefan Schneider, Stephan Deplazes, Yonis Ahmed, and Ashlee Quintana presented at the 2022 AFOSR review meeting (virtual) "From deep eutectic solvents to sustainable propellants" May 24-26, 2022.

3. Chambreau, S. D., "Next-Generation Liquid Propellants", AFRL Inspire, May 22, 2022, Wright-Patterson AFB, OH.
4. Steven D. Chambreau, Heterogeneous Catalysis of Ionic Liquids, presented at the American Chemical Society Spring 2022 National Meeting, March 20-24, 2022, San Diego, CA.
5. Liu, Jianbo; Zhou, Wenjing; Chambreau, Steven D.; Vaghjiani, Ghanshyam L. "Computational investigations into hypergolic ionic liquid reactions using VENUS direct dynamic trajectories, kinetics modeling and product spectroscopy simulations" Symposium in honor of William Hase, 261st ACS National Meeting (virtual), April 5-16, 2021.
6. Dr. Schneider organized a virtual workshop for AFOSR on the theoretical determination of critical physical properties of highly-conductive liquid propellants, 17th Febuary 2021.
7. Dr. Schneider served as a key note speaker during an AFOSR workshop on the theoretical determination of critical physical properties of highly-conductive liquid propellants, "IL, Deep Eutectic Propellants, Dual Mode Propellants", 17th Febuary 2021
8. Dr. Schneider presented an invited lecture on a transition success story "From an interesting molecule to a propellant to a mission capability" at the inaugural USSF/AFOSR Space Sciences Summit (SSS) that was held virtually 13-14 Oct 2020.
9. Depew, Daniel; Wang, Joseph J.; Chambreau, Steven D.; Boatz, Jerry A.; Vaghjiani, Ghanshyam L. "Proton mobility in aqueous hydroxylammonium nitrate: New insights and implications" 260th ACS National Meeting (virtual), August 23-27, 2020.
10. Zeng, Helen J.; Khuu, Thien; Chambreau, Steven D.; Boatz, Jerry A.; Vaghjiani, Ghanshyam L.; Johnson, Mark A. "Molecular-level aspects of ionic liquid reactivity via structural characterization of cationic ionic liquid clusters by cryogenic vibrational spectroscopy and calculations" 260th ACS National Meeting (virtual), August 23-27, 2020.
11. The annual AFOSR review meeting was held as a virtual meeting during its intended date of May 19-21, 2020. Dr. Schneider gave an invited presentation, laying out opportunities, challenges and Air Force needs in regards to the groups research focus of "DES and SILs: Improving Energetics by Applying Modern Concepts".
12. Dr. Schneider presented an invited lecture at the AFOSR champion shipped AFRL Chemistry Forum Webinar on "DES and SILs: Improving Energetics by Applying Modern Concepts" April 15, 2020.

5.0 Extended Scientific Visits From and To Other Laboratories

Dr. Chambreau: X-ray photoelectron spectroscopy experiments investigating coking in supercritical hydrocarbon fuels at the Molecular Foundry, Lawrence Berkeley Laboratory, January 27-February 1, 2020.

Dr. Chambreau: High-speed x-ray imaging of monopropellant thruster experiments at the Advanced Photon Source, Argonne National Laboratory, March 6-11, 2020.